8-2018

Demonstrator for Selectively Compliant Morphing Systems with Multi-stable Structures

David M. Boston
Purdue University

DEMONSTRATOR FOR SELECTIVELY COMPLIANT MORPHING SYSTEMS WITH MULTI-STABLE STRUCTURES

A Thesis

Submitted to the Faculty

of

Purdue University

by

David M. Boston

In Partial Fulfillment of the

Requirements for the Degree

of

Master of Science in Aeronautics and Astronautics

August 2018

Purdue University

West Lafayette, Indiana

THE PURDUE UNIVERSITY GRADUATE SCHOOL
STATEMENT OF THESIS APPROVAL

Dr. Andres Arrieta, Chair

School of Mechanical Engineering

Dr. William Crossley

School of Aeronautics and Astronautics

Dr. Tyler Tallman

School of Aeronautics and Astronautics

Approved by:

Dr. Weinong Chen

Head of the School Graduate Program

To Grandpa. Thank you for giving me the bug. And to Mom and Dad. Thank you for helping me chase it.

ACKNOWLEDGMENTS

The author would like to acknowledge the assistance and contributions of all of his colleagues in the Programmable Structures Lab at Purdue. Thanks must also be extended to Professor Andres Arrieta for the constant guidance and advice and Professor William Crossley for providing the initial introduction and help in preparing for the Thesis Defense. This work was made possible through Grant FA9550-17-1-0074 On-demand Stiffness Selectivity for Morphing Systems provided by the Air Force Office of Scientific Research. The author would like to express his sincere gratitude to Dr. Byung Lip (Les) Lee for his support through the administration of this grant.

TABLE OF CONTENTS

LIST OF TABLES

LIST OF FIGURES

ABBREVIATIONS

ABS	Acrylonitrile Butadiene Styrene
ALLSE	Full-model Strain Energy
CLT	Classical Lamination Theory
FDM	Fused Deposition Modeling
FEA	Finite Element Analysis
MADCAT	Mission Adaptive Digital Composite Aerostructure Technologies
NACA	National Advisory Committee for Aeronautics
NASA	National Air and Space Administration
PLA	Polylactic Acid
PVA	Polyvinyl Alcohol
SLA	Stereolithography
T.E.	Airfoil trailing edge
TPU	Thermoplastic Polyurethane

ABSTRACT

Boston, David M. MSAAE, Purdue University, August 2018. Demonstrator for Selectively Compliant Morphing Systems with Multi-stable Structures. Major Professor: Andres F. Arrieta.

The field of morphing wings presents significant potential for increasing the efficiency of aircraft. Conventional designs used in the industry limit the adaptability of aerodynamic surfaces to address an engineering trade-off between load-carrying and compliance. This same trade-off remains a factor in morphing wings, which must also balance weight considerations while attempting to remain competitive with conventional designs. The current state-of-the-art in morphing wings is briefly described in this work. This is followed by an investigation into a new application of the principle of selective stiffness, by which local changes in stiffness may be applied to affect the global structural characteristics. In this manner, this trade-off is addressed by providing the ability to allow a deformation mode when undergoing shape change and restrict it when sustained load-carrying is required.

This principle has previously been explored using pre-stressed composite laminates to produce a bi-stable structure with unique curvature in each stable state. Geometrically bi-stable structures are explored for the same purpose in this research. Three types of bi-stable element are explored and presented. The last of these is then embedded in a simple airfoil concept. The placement and geometry of this element are optimized, and a physical model is produced using additive manufacturing. This physical model is finally mechanically tested to assess the stiffness in each stable state of the embedded element.

1. INTRODUCTION

Modern aircraft are typically designed for a single purpose. They employ rigid structures to support aerodynamic loads experienced in pursuit of their intended mission. However, even aircraft with one function face a variety of operating points over the course of a flight, for example takeoff, climb, cruise, descent, and landing. Each operating point expresses its own aerodynamic conditions and structural requirements. Encompassing all of these points into a rigid structure severely limits the design space available to engineers. This results in sub-optimal designs for each operating point, yielding an overall inefficient design. Lifting devices such as flaps are used in conventional aircraft design to reconcile some of the trade-offs and provide a more expansive design space. These devices introduce their own inefficiencies, however, by disrupting smooth airflow around the wing and increasing drag.

The need for increasingly efficient solutions is a driving force in modern aircraft design. Energy consumption will naturally increase with the growing global population. One model predicts an approximately fifty percent increase in transportation energy consumption, with jet fuel as the second-largest growing energy source [1]. This increase is coupled to an expectation of continual growth of the airline industry and increasing energy cost [2]. Optimizing the aerodynamic properties of an airfoil at any given moment in flight and eliminating sources of parasitic drag will be critical to improve the efficiency of future aircraft.

The discipline of wing morphing seeks to provide alternative solutions to the trade-offs encountered when limiting the shape of an aircraft to a single, static design. Each operating point in a morphing system can be represented by its own set of optimal of design parameters. Morphing systems in practice, however, are often subject to their own design constraints and trade-offs that limit their usefulness in general aircraft design. The focus of this work is the development of a concept aerospace structure

which utilizes localized structural instabilities to induce global changes in structural stiffness. In this manner, a wing may demonstrate a compliant state, in which it may be deformed to allow for changes in aerodynamic properties, and a rigid state, in which it can resist aerodynamic loading.

This concept was first developed utilizing composite laminates which develop internal stresses during cooling that allow them to switch between two stable states, each with a unique geometry [3]. The current project continues this work with the development of topologies that enable a structural element to demonstrate this bi-stable characteristic using curved geometries, rather than internal pre-stress. This provides additional possibilities for manufacturing the elements embedded in a monolithic structure. The goals of this project are then:

- Investigating the manufacturing of curved stress-free truss-like compliant structures to exhibit geometrically driven multi-stability when deformed by an external force, as in the case of an arch.
- Studying the effect of adding a shrinking layer to the stress free curved structure to induce a pre-stress field leading to multi-stability after additive manufacture of the compliant structure.
- Designing a selectively compliant morphing demonstrator.
- Manufacturing and testing of the selectively compliant morphing section under simulated structural loads.

The theoretical basis of this project is provided in Chapter 2, as well as information on the state-of-the art that this project builds upon. Chapter 3 discusses initial element designs utilizing singly and doubly curved shell geometries. Chapter 4 provides an analysis of a singly curved shell with flexural reinforcement that is additionally embedded in a NACA0014 airfoil. This airfoil structure is further developed in Chapter 5 using a response surface method optimization. The manufacturing and mechanical testing of these elements in isolation and embedded in the airfoil is presented in Chapter 6.

1.1 Scientific Contribution

The following papers were written and published over the course of this project:

- Boston, D. M., and Arrieta, A. F., 2018. "Design of monolithic selectively compliant morphing structures with locally bistable elements. In 2018 AIAA/AHS Adaptive Structures Conference, AIAA SciTech Forum, American Institute of Aeronautics and Astronautics. doi:10.2514/6.2018-1064.

- Boston, D. M., Arrieta, A. F., and Rivas-Padilla, J., 2018. "Monolithic morphing rib with selective stiffness from embeddable bi-stable elements". In 2018 Smart Materials and Adaptive Structures Conference, American Society of Mechanical Engineers. Accepted for publication as of this writing.

2. BACKGROUND AND STATE-OF-THE-ART

Altering the shape and structure of the wing to induce changes in aerodynamic properties dates back to the earliest days of flight. The initial patent received by the Wright Brothers consisted of a method for in-flight control by means of warping the wings, the goals of the apparatus being:

> To provide means for maintaining or restoring the equilibrium or lateral balance of the apparatus, to provide means for guiding the machine... and to provide a structure combining lightness, strength, convenience of construction, and certain other advantages [4].

The wings of the Wright Flyer use a network of wires attached to struts at the wingtips to create a torque on the wings, changing the angle of attack at the wingtips. The materials used in the Flyer, wood and canvas, were compliant enough to withstand this torque without failure or permanent deformation. In this manner, they were able to create a multi-functional, lightweight structure that could provide control and stand up to aerodynamic control.

History has shown, however, that the increased loads of larger, heavier aircraft, going continually faster, requires greater strength than can be achieved using wood and canvas. The use of stronger materials and more rigid structures naturally precludes the deformability necessary for shape-adaptation. The task separation principle is thus adopted in conventional wing design. This concept was originally postulated by Sir George Cayley as a means of making powered flight viable by separating thrust and lift, but also allows for strong wings that can withstand the increased demands of higher wing loading [5]. Two discrete bodies are utilized to either provide strength or adaptability. These are then coupled together using a single degree of freedom into a device capable of providing lift. Task separation places constraints on the design,

such as limiting movement to a single degree of freedom and the requirement of a discontinuous aerodynamic surface. This helps to resolve design conflicts, but this is at the cost of an overall reduction of the design space. This prevents the realization of potentially more optimal designs.

Recent trends in morphing aircraft design have emphasized a return to multi-functional structures [6]. The development of new materials, particularly high-strain composites, has provided new opportunities for exploring designs spaces previously restricted by conflicts in strength and deformability. A natural trade-off still exists in morphing aircraft, however, between the need to maintain a shape under load and change the shape to meet the needs of multiple operating conditions. This trade-off is explored further in the next section of this chapter, along with several designs both historical and recent that attempted to rectify this conflict. The subject of on-demand selective stiffness is then presented as an alternative to these designs. The foundations of this concept in the field of bistable laminate plates and the previous work in this area that this project builds upon are also provided.

2.1 The Morphing Trilemma

The inherent compromise between the ability to retain a shape under load and deform when desired is the central problem of the field of morphing wings. This is addressed in conventional designs by utilizing mechanisms that separate the tasks into multiple sub-components, as previously discussed. This introduces a new penalty to the trade-off, however, in the form of increased weight from the rigid structure and mechanisms to drive a second rigid body for shape change [5]. Figure 2.1 shows this relationship graphically. As the figure points out, each desirable characteristic is achievable in combination with another, and examples exist in the literature and practice that show this, but this is only accomplished at the cost of a third characteristic.

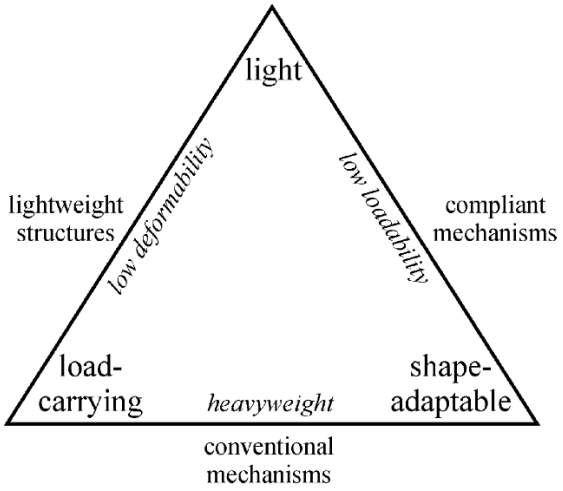

Figure 2.1. Graphic depiction of the trade-offs faced by morphing structures, the "Morphing Trilemma" [5].

References [5,6] go into detail on how designers throughout history have attempted to address the problem of morphing. The latter of these treats morphing in a very general sense, while the former focuses primarily on changes in the airfoil cross section, which is the focus of this work. Most concepts developed historically have fallen into the "convential mechanisms" category, such as the airfoil shown in Fig. 2.2. These concepts tend to incorporate trusses and linkages that can be actuated to deform a compliant skin (Fig. 2.2(a)), flap-like bodies, or discrete sections of the airfoil (Fig. 2.2(b)). The complexity of these mechanisms adds weight, as previously suggested, and the many moving parts makes them difficult to maintain.

More recent research and development in morphing structures has focused on another category, specifically compliant mechanisms. This class of structure is categorized by parts that rely on elastic deformations of the structure itself, rather than the relative motion of structural components [9]. The idea of a compliant structure with a piezoelectric actuator was proposed as early as 1990. The initial study demonstrated the theoretical advantages of incorporating the piezoelectric actuator into a laminated composite skin for aeroelastic tailoring and control [10]. Although no physical model was produced in that study, the idea has become commonplace in

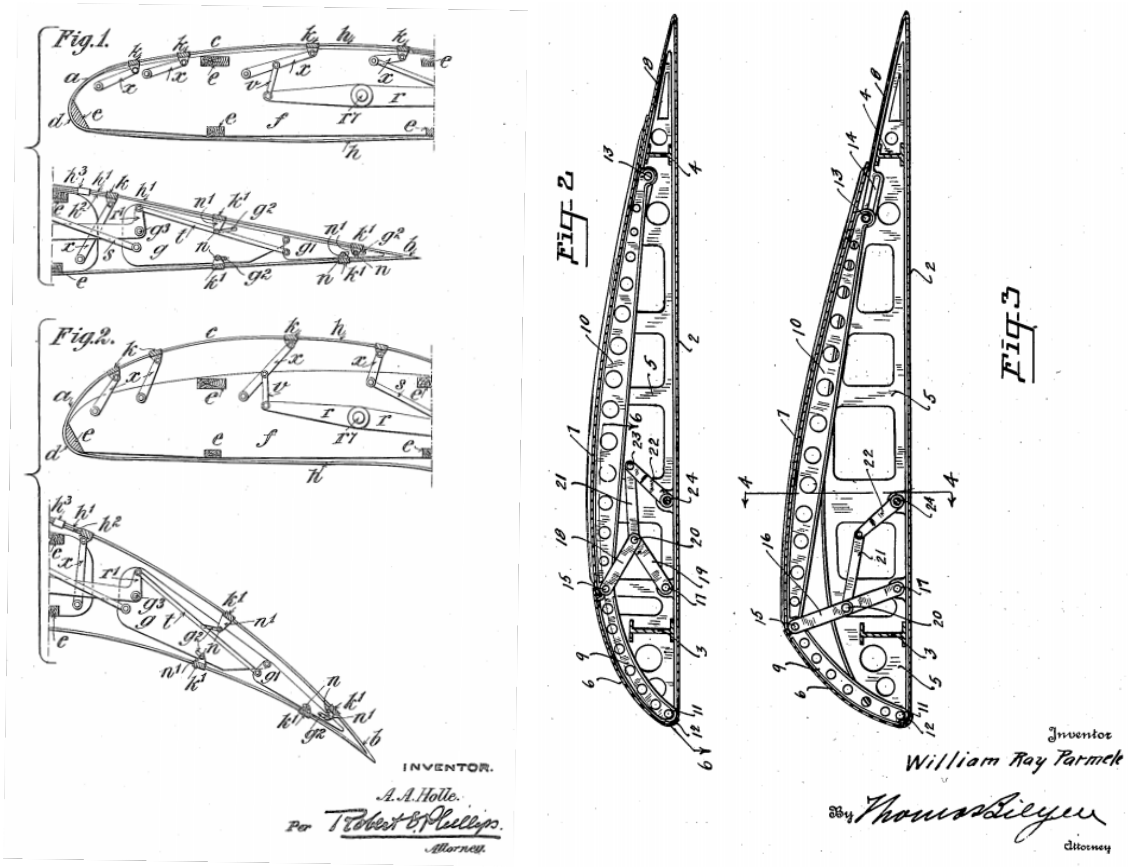

(a) (b)

Figure 2.2. Morphing wing concepts patented by (a) Holle in 1917 [7] and (b) Parmele in 1931 [8] .

morphing technologies. Its use is seen, for example, in an active trailing edge concept developed for rotorcraft, seen in Fig. 2.3 [11]. This concept utilizes a contracting actuator in the middle of the trailing edge to buckle a composite laminate skin, creating a change in the camber line of the trailing edge section of the airfoil.

Another example of a compliant structure is seen in Fig. 2.4. This idea, proposed by Hasse, Zuest, and Campanile in 2010, is derived from a so-called belt-rib concept. This refers to the continuous deformable outer skin, the belt, and the truss-like network of members composing the rib [9]. The authors of this study used a modal analysis coupled with an optimization procedure to match a compliant structure to

a set of specified deformation modes, in a process they dubbed selective compliance (the use of this definition is discussed in the next section). The use of this structural technique, as well as the similar concepts of lumped or distributed compliance, are discussed at length in [5, 12].

The Mission Adaptive Digital Composite Aerostructure Technologies (MADCAT) concept developed by NASA was presented in 2017. MADCAT uses a three-dimensional network of members (see Fig. 2.5) which provide compliance solely in torsion along the span [13]. This allows a tube to rotate the wingtip, causing the wing to warp, and changing the local angle of attack along the span, much the same way as the Wright Brothers' original Flyer.

The disadvantage of these concepts is inherent in their compliance, which requires an expenditure of energy from an actuator to maintain their shape and resist aerodynamic loading. The goal of this work is to propose a multi-functional structure that allows for both shape-adaptability and load-carrying without the added weight of conventional mechanisms, providing a solution to the so-called morphing trilemma.

Figure 2.3. Active Trailing Edge concept proposed by Grohmann, et al. in 2008 [11].

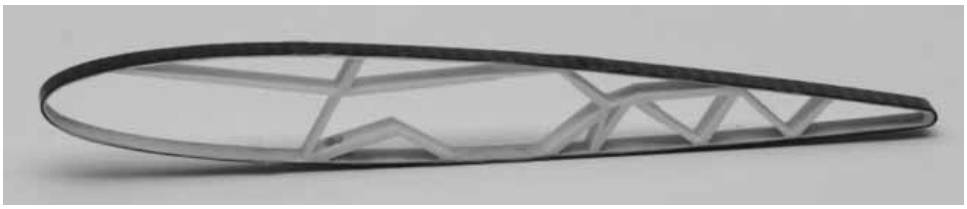

Figure 2.4. Compliant airfoil using a belt-rib concept developed by Hasse, Zuest, and Campanile in 2010 [9].

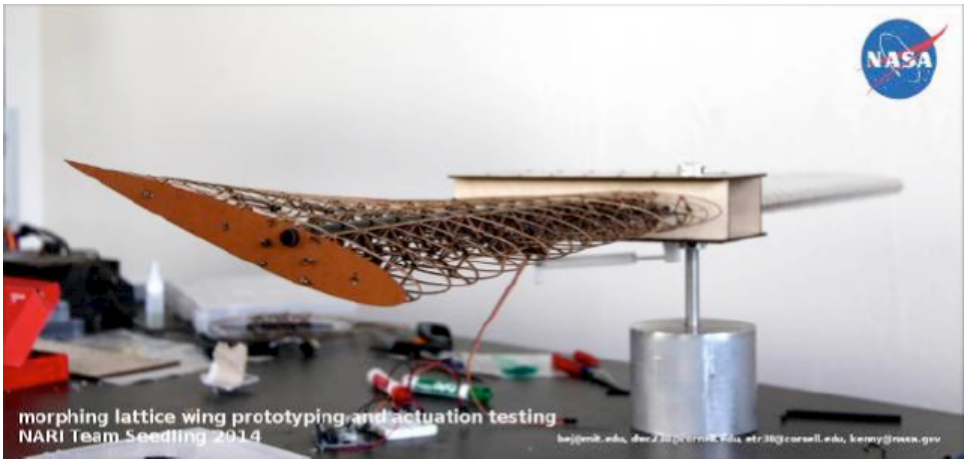

Figure 2.5. Morphing wing using compliant lattice to allow span-wise warping [13].

2.2 Selective Stiffness

The term selective stiffness (analogous to selective compliance as the inverse of stiffness) has previously been used to refer to a type of compliant structure that restricts deformation to a set of specified modes [9]. This definition places the structural behavior as a subset or hybrid of distributed and lumped compliance. For the purposes of this work, however, this fails to accurately capture the programmatic nature of the behavior described here. The selective stiffness referred to in this research is a switchable property of the system. It describes two or more stable states or configurations that have a unique value of stiffness. This can in turn restrict or allow specified deformations when combined with a system of distributed compliance.

The definition used here is also notably distinct from what is commonly referred to as variable stiffness, in which the stiffness changes in response to a stimulus, often as a result of post-buckling [14] or other non-linear behavior. This kind of behavior is presented in [15], for example, as a non-linear, continuous stiffness decrease in response to increasing aerodynamic load as a passive gust-alleviation method, demonstrated in Fig. 2.6. The trend, however, is a tailoring of the local stiffness response with regards to a global stimulus as opposed to the distinct states observed in this study, independent of the global loading.

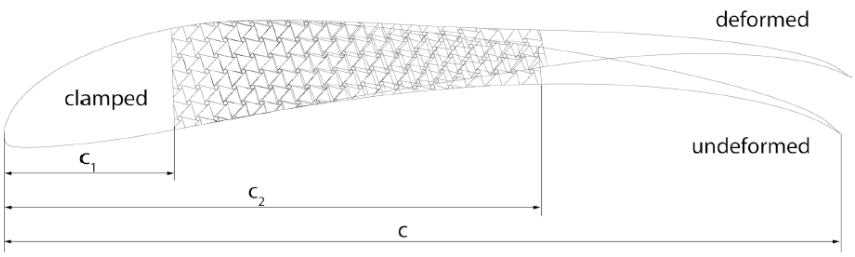

(a)

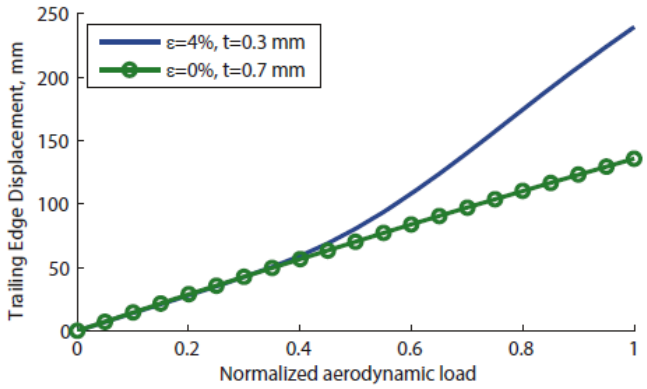

(b)

Figure 2.6. (a) Schematic representation of a variable stiffness airfoil proposed by Runkel, et al in 2017 with (b) the stiffness response versus aerodynamic load based on curvature of elements making up the cellular structure of the airfoil [15].

The characteristic switchability observed in this study is the result of an elastic instability commonly found in post-buckling phenomena. In the classical study of beam buckling, shown in Fig. 2.7(a), a bifurcation point exists in the stability of the beam after a critical axial load is exceeded. Each branch of the bifurcation may be accessed by a transverse displacement forcing a snap-through instability. The axial response to the load post-buckling is symmetric in the classical case, however. This behavior can be altered by changing the properties of the beam to yield an asymmetric response [3]. The axial stiffness of the beam in this case differs according to the branch of the bifurcation (see Fig. 2.7(b) and (c)). The snap-through phenomenon may then be used to select the desired stiffness for a given scenario.

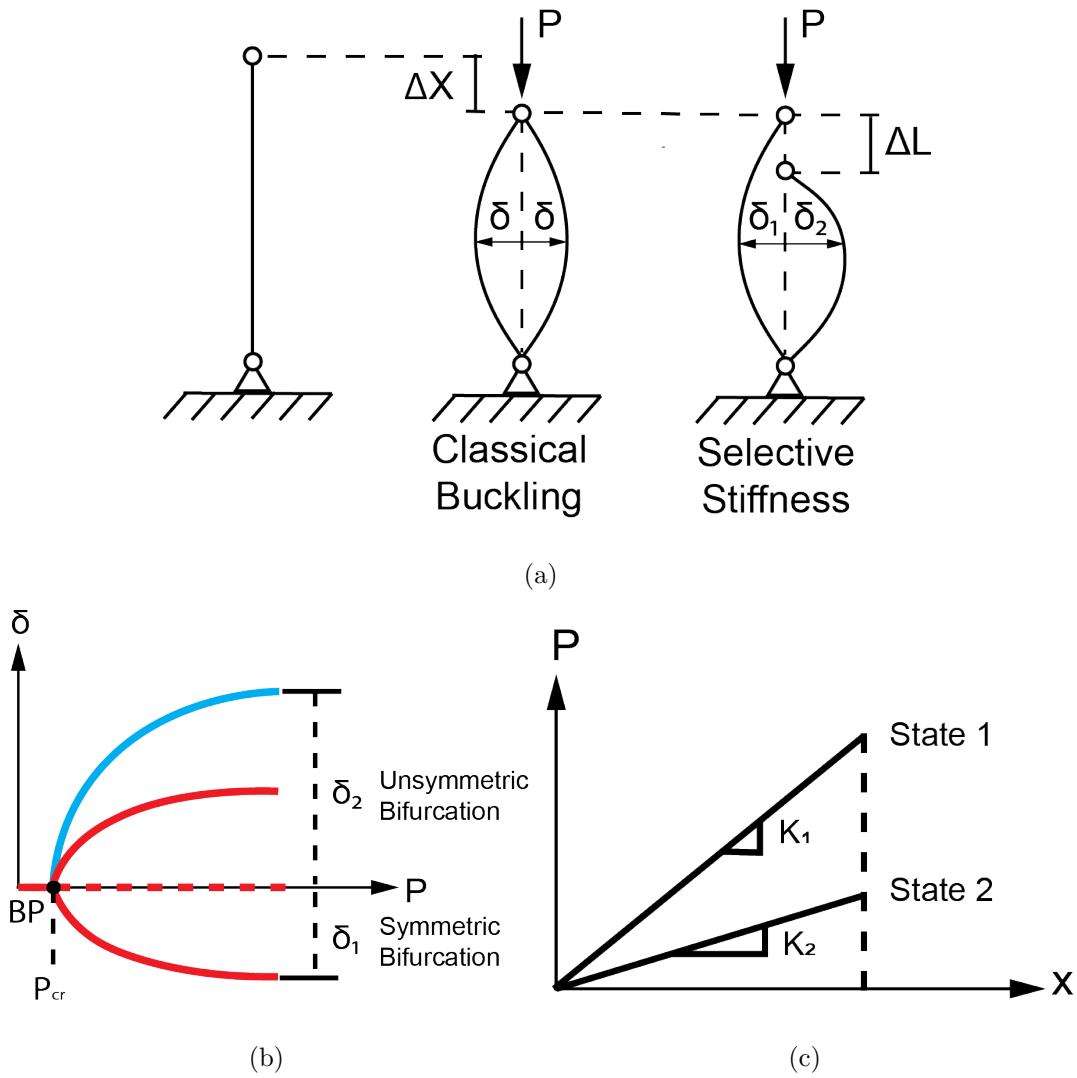

Figure 2.7. Selective stiffness based on the buckling of beams: (a) diagram of classical and asymmetric buckling which yields (b) a bifurcation diagram with asymmetric divergence that results in (c) unique force-displacement responses for each divergence path [16].

This principle was implemented in a morphing rib concept using laminated composite plates with an unsymmetric layup [17]. The resulting curved shells demonstrated two stable shapes with a unique stiffness, either flexible or rigid. A physical model, shown in Fig. 2.8, integrated two of these elements and provided measurements of the force response to a vertical deflection of the trailing edge. The resulting

stiffness of the elements in rigid and flexible modes could then be calculated, yielding a ratio of 2.47 times greater stiffness in the rigid configuration.

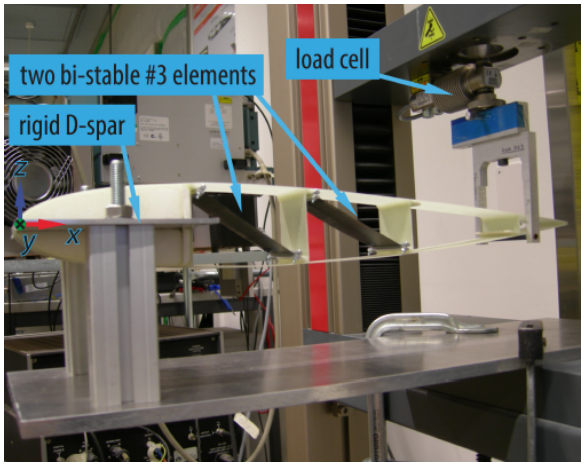

Figure 2.8. Photo of selectively stiff airfoil in testing apparatus [17].

2.3 Bi-stability

As previously mentioned, the ability to switch between desired stiffnesses is dependent on the existence of two stable states, known as bi-stability. This phenomenon derives from a series of minima in potential energy when subjected to some loading condition, shown for example in Fig. 2.9. Each local minimum is separated by a corresponding local maximum, which represents an energy barrier between stable states. This takes the form of a dynamic snap-through instability in the case of structural elements. An element that demonstrates asymmetric behavior, as shown in the graph, will display different properties in each of its stable states [18].

Interest in this phenomenon and its occurrence in composite laminate plates began as early as 1980 [19]. It was observed that laminate plates with an unsymmetric layup would warp due to the mismatch of thermal expansion properties in the anisotropic material. However, the findings for thin plates do not match those predicted by Classical Laminate Theory (CLT). The resulting shells instead display a cylindrical

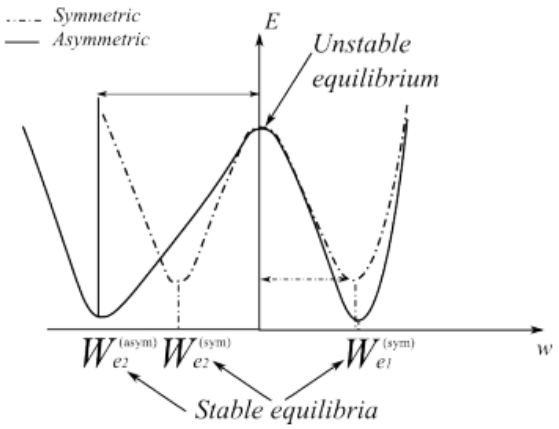

Figure 2.9. Graph showing potential energy basis for bi-stability [18].

curvature with a dynamic snap-through between two stable shapes with curvatures along the principal fiber directions. This phenomenon has been further investigated, and an analytical model has been developed to predict the stability behavior, accounting for the failure of CLT to do so [20].

Considerable work has been done investigating the characteristics of these unsymmetric laminate shells [21–23]. They have found use as selectively stiff elements in a truss-like structure, as discussed. However, these elements suffer from a manufacturing sensitivity and face limits in their application within monolithic structures based on current technologies and methods [17]. The focus of this study is therefore on achieving bi-stability based upon the geometry of curved shells, rather than pre-stress induced by the mismatch of thermal expansion during manufacturing.

Geometric bi-stability is common in so-called "von Mises truss" designs used in switchable mechanical devices [24]. The stability of similar beam-like devices, often found in microelectromechanical systems, has also been explored [25]. The elements found in the subsequent chapter, however, draw from the stability of curved shells, a theoretical framework for which can be found in [26–28]. This technique has also been explored in tape springs, sometimes found in deployable space structures [29–31].

3. BI-STABLE ELEMENTS DERIVED FROM CURVED GEOMETRIES

This chapter is based on the conference contribution:

D. M. Boston, A. F. Arrieta: "Design of monolithic selectively compliant morphing structures with locally bistable elements". In 2018 AIAA/AHS Adaptive Structures Conference, AIAA SciTech Forum, American Institute of Aeronautics and Astronautics. 2018.

DOI: 10.2514/6.2018-1064.

And the conference contribution selected for publication at the time of writing:

D. M. Boston, A. F. Arrieta, J Rivas-Padilla: "Monolithic morphing rib with selective stiffness from embeddable bi-stable elements". In Proceedings of the ASME 2018 Conference on Smart Materials, Adaptive Structures and Intelligent Systems, SMASIS 2018, American Society of Mechanical Engineers. 2018.

Three element geometries were explored over the course of this project. The goal for each element was to demonstrate bi-stability based solely on geometry. The element then needed to be embeddable as a member in a truss-like structure and demonstrate noticeably different "axial" stiffness (referred to here also as stiffness in the plane of the element). The elements are presented in chronological order of development: using variable curvature perpendicular to the length of the element, constant curvature in both directions, and curvature perpendicular to the width of the element with flexural reinforcement in-plane (also referred to here as a slit-plate element). A finite element analysis (FEA) was carried out for each element, with a more detailed parametric

study conducted for the latter two. Only the last element met each requirement and was incorporated into an airfoil design as described in the next chapter.

3.1 Variable Curvature in One Direction

Bi-stability can be derived from prestress within the structure or its geometric properties. In this section, the design and simulation of a bi-stable element given a prestress after being manufactured stress-free is described. The element is composed of a shell with transition regions and a primary region with varying curvature along its primary axis.

3.1.1 Geometry Description

In this work, we initially utilized previously designed bi-stable shell geometries from unsymmetrically laminated composites which exhibit pre-stress after manufacturing [3,32]. This is illustrated for the parametric geometry of a bi-stable element, as shown in Fig. 3.1. A parametric model is created and analyzed using FEA carried out in the commercial software package Abaqus to determine its stability characteristics.

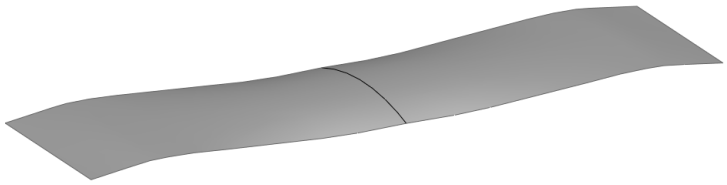

Figure 3.1. Parametric geometry for bi-stable element with variable curvature in one direction.

The model consists of four regions mirrored about the middle of the member, shown in Fig. 3.2a. The edge of the member is a flat region which is inclined with respect to the members neutral plane. Next is a transition region with a small, constant curvature. This leads into a curved section that is parallel to the neutral

plane, as shown in Fig. 3.2b. The curvature, κ, in this section is defined by a linear relationship $\kappa(\hat{x}) = a\hat{x}$, where $\hat{x}$ is in the lengthwise direction, shown in Fig. 3.3. A section of constant curvature then allows for a smooth transition between mirrored halves of the member. The parametric nature of the model allows for an exploration of the design space to find the optimum geometry for the in-plane stiffness of two stable states.

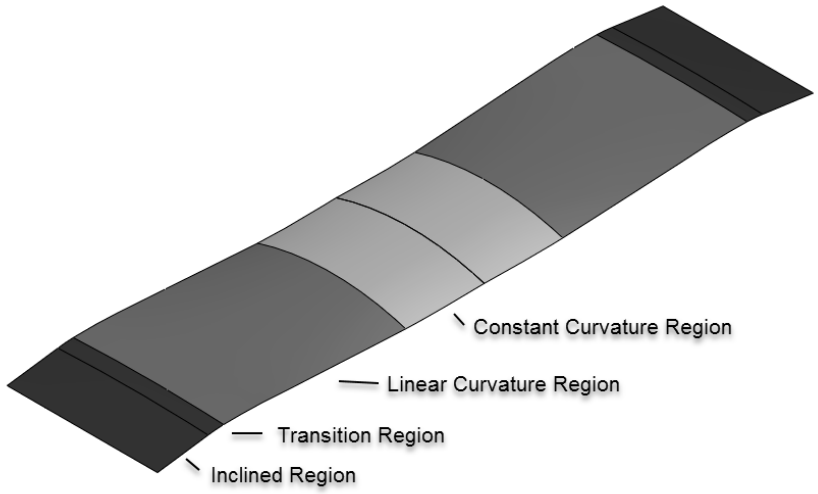

(a)

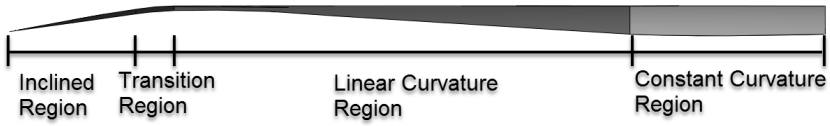

(b)

Figure 3.2. (a) Isometric view and (b) side view showing regions driving geometry.

3.1.2 Finite Element Model

An initial assessment of the bi-stability of the member is carried out analyzing a specific finite element (FE) model of the element. A 10 mm wide by 43 mm long member was generated from the parametric model. It was given a 10 degree initial

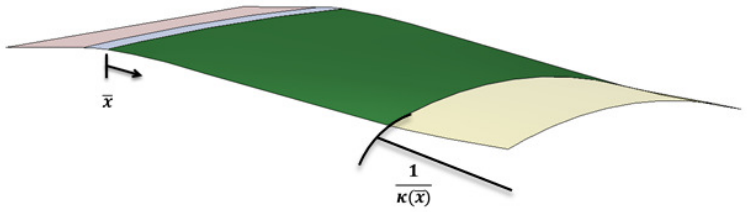

Figure 3.3. Image describing formation of curvature in model.

incline of 3.4 mm. The transition region was given a radius of 6 mm in the lengthwise direction, with a curvature of κ=0.01. The curving region of the member was 12.2 mm long with curvature $a = 0.005$. The constant curvature region was 5.2 mm in length. These parameters were chosen to mimic the composite laminate known to be bi-stable and to fit in a rib model also being developed.

The geometry of the member was imported into Abaqus and given a mesh. Symmetry was used in the lengthwise direction for computational efficiency. The mesh was generated from S4R elements approximately 0.4 mm on each side. This resulted in a relatively fine mesh of 1540 elements, shown in Fig. 3.4. The elements were chosen to be 0.5 mm thick. The material properties for the model were an elastic modulus of 3 GPa and Poissons ratio of 0.3, to reflect the properties of generic plastics often found in additive manufacturing applications.

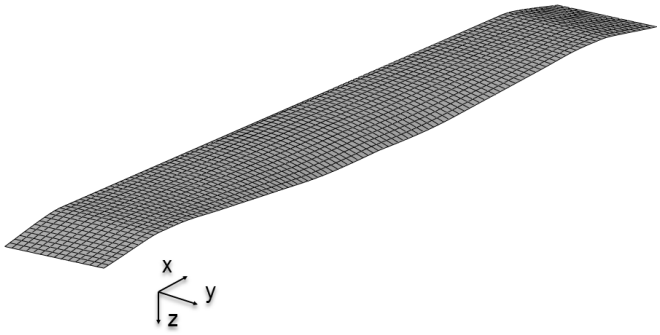

Figure 3.4. Mesh generated for bi-stable member.

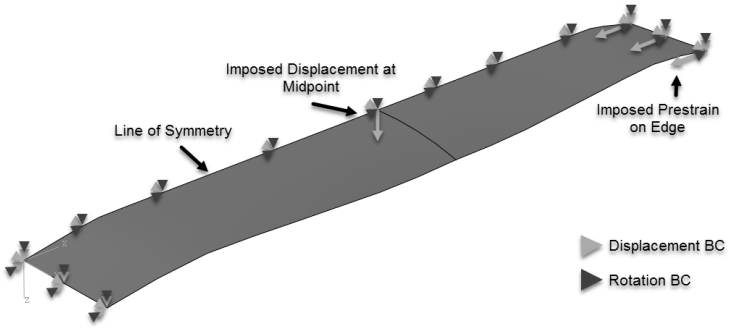

Figure 3.5. Schematic representation of boundary conditions used in Abaqus model.

The bi-stability of the member was tested by restricting the movement at the flat edges of the plate. On one end, all but rotation about the edge were restricted to represent a pinned condition. On the other end, lengthwise motion was also allowed to represent a sliding condition. A symmetric boundary condition was placed on the line of symmetry. A translation boundary condition in the out-of-plane direction was then imposed on the middle of the line of symmetry in order to force the member to transition between states. A summary of the boundary conditions used in the model can be seen in Fig. 3.5. Analyzing the model results indicated that for the chosen geometry of the element bi-stability was not found. To address this the lengthwise motion of the sliding end is changed to a specified displacement to represent a pre-strain of the model. This prestrain represents an elastic interaction with a separately produced morphing structure or the introduction of an additional elastic element with an equivalent strain energy. After the influence of a prestraining layer is accounted for, the element developed a second stable state. The influence of a prestraning layer is further studied by generating strain energy-displacement curves from the analysis output, shown in Fig. 3.6. It can be seen that for the prestraining layer a minimum value above 0.2 % prestrain is necessary for bi-stability to occur. The stable geometries of a representative bi-stable element obtained with 0.3 % prestrain are shown in Fig. 3.7.

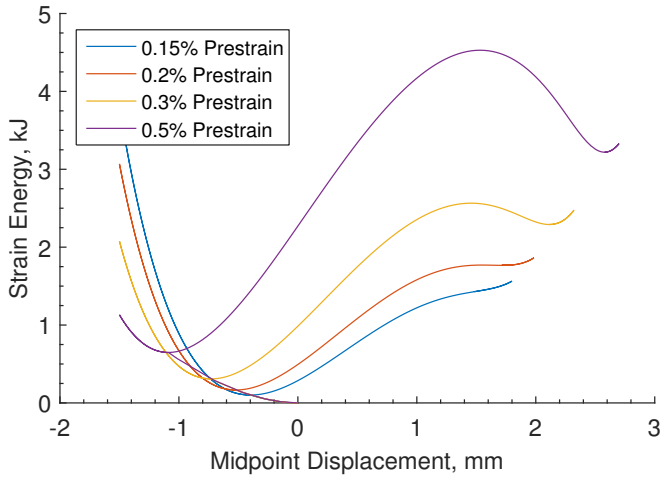

Figure 3.6. Strain Energy - Displacement curves for increasing values of prestrain.

(a) (b)

Figure 3.7. Results of Abaqus analysis showing stable states of (a) prestrained structure and (b) buckled structure for 0.3 % prestrain.

3.1.3 Fused Deposition Model

Using the same parameters as the finite element model, a physical sample is manufactured using Fused Deposition Modeling (FDM). An Ultimaker 3 printer is used to create the model using polylactic acid (PLA) filament. The Cura slicing software associated with Ultimaker is used to generate the print file with the software's "Extra Fine" default settings. The model was initially printed on the long edge to avoid using support material that would cause imperfections in the surface. Later samples were printed flat using a water-soluble support material (polyvinyl alcohol (PVA)). An example of the model is shown in Fig. 3.8. The model demonstrates its second stable condition in Fig. 3.8b when a prestrain is applied, causing the element to buckle. This is even in the clamped condition shown here, which demonstrates that

the element can be embedded in a structure and retain its bi-stability, provided a prestrain can still be applied.

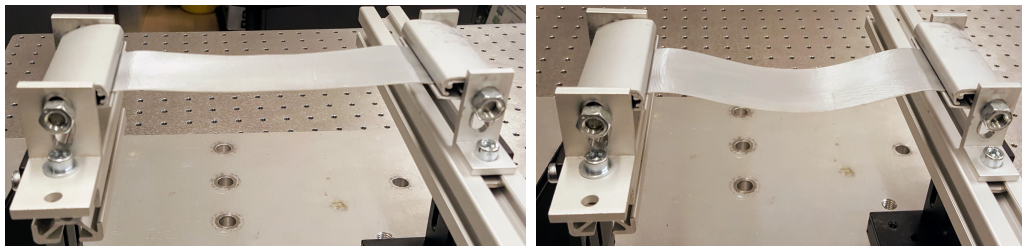

(a) (b)

Figure 3.8. Printed model in (a) unstressed configuration and (b) stable, buckled structure.

The results show that pre-stress is necessary to obtain bi-stable behavior in this class of structural elements, which can be built during additive manufacturing or as an external step as shown above. Nevertheless, an approach simplifying the manufacturing of multistable elements that does not rely on prestraining techniques is desirable. This is explored in the following sections.

3.2 Constant Curvature in Two Directions

Elastic theory predicts that, for shells of constant curvature, a second stable shape exists when the curvature is inverted. This principle is applied in this section to develop an element with a doubly curved shell. We describe the element's geometry and present a printed proof-of-concept model showing the element's bi-stability. We then discuss a parameter study conducted to explore the design space of this element and address the element's embeddability in a morphing structure.

3.2.1 Geometry Description

The geometry of this bi-stable element exploits that of a doubly curved shell of constant curvature. As such, the general topology of the shell can be mathematically

described by that of a torus. A section of the torus, shown for example in Fig. 3.9, makes up the central region of the element. A planar region connects the edge of the curved torus section to an inclined region, similar to that found in the single curvature model previously described. This results in the model shown in Fig. 3.10.

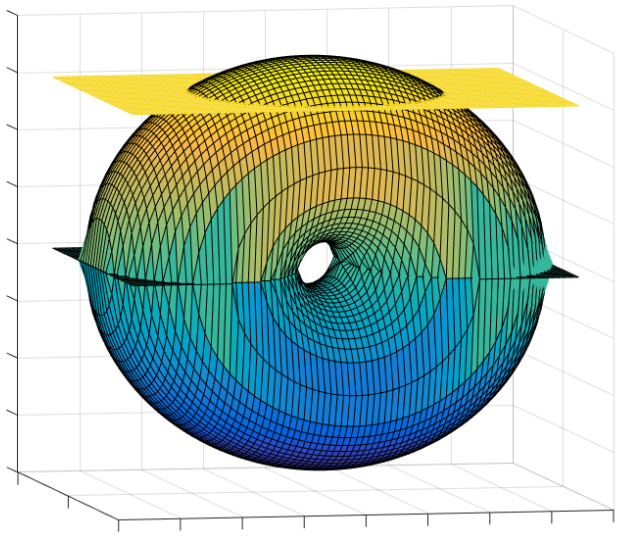

Figure 3.9. Depiction of torus section used in bi-stable element.

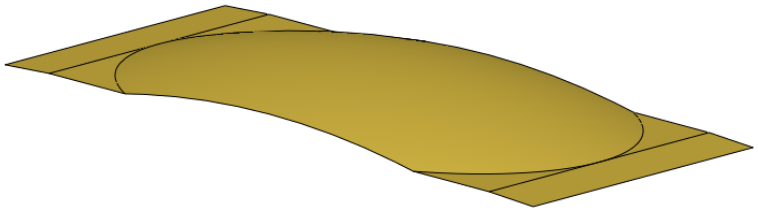

Figure 3.10. Depiction of doubly curved bi-stable element.

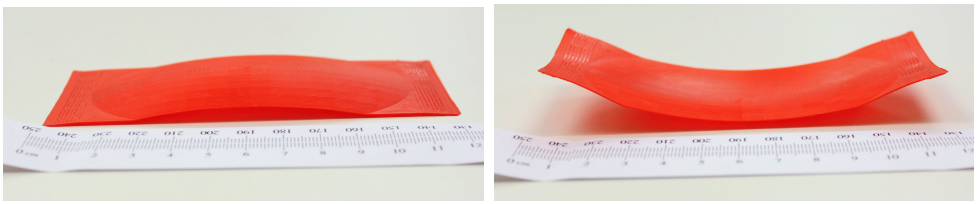

(a) (b)

Figure 3.11. Printed model in (a) stable state as manufactured (b) deformed stable state.

3.2.2 Proof-of-Concept Model

A model is printed using this geometry in order to prove that it could demonstrate bi-stability. The Ultimaker 3 printer is used with PLA filament, using the "Extra Fine" settings in the Cura software. The model is printed flat using PVA supports to prevent damage to the surface during removal. A model is also printed on the long edge, as before; however, stresses during deformation cause the deposited layers to separate, forming cracks in the surface. The printed result, shown in Fig. 3.11a, demonstrates a second stable shape when the corners are displaced in opposition to the torus region, shown in Fig. 3.11b. Unlike the previous element, which demonstrates a behavior similar to traditional beam buckling when prestrained and deflected, this element exhibits a much more dynamic snap-through behavior. This is typically expressed by an initial buckling and inversion of one side of the curved region, which "rolls" through to the other side until the whole curve is inverted. In the physical model, this roll can happen quickly, but requires a continuous load throughout the duration of the snap in order to reach the second stable state. If the load is removed before the majority of the curved region is inverted, the element reverts to its original state.

3.2.3 Finite Element Model

A finite element model for analysis of the double curved bi-stable elements is established using Abaqus. Eleven parameters are identified in the proof-of-concept model, hereafter referred to as the control model. A list of these parameters and their associated values are given in Table 3.1 and are visually identified in Fig. 3.12. Throughout the finite element analysis, an elastic modulus of 3 GPa, approximating the value of PLA given by Ultimaker, is used. Data on Poisson's Ratio for PLA filament is not given by manufacturers and is inconsistent from third party sources, so an assumed value of 0.3 is used.

Table 3.1. Parameters and control values for the doubly curved element model.

Parameter	Value
Element Width	50 mm
Element Length	120 mm
Short Edge Radius	80 mm
Long Edge Radius	100 mm
Torus Region Length	100 mm
Planar Region Length	0 mm
Inclined Region Length	10 mm
Inclined Region Angle	3 degrees
Torus Region Thickness	0.4 mm
Planar Region Thickness	0.4 mm
Inclined Region Thickness	0.4 mm

After geometry is generated using the control parameters, the element is meshed using Abaqus's meshing algorithm. In order to account for the curvature, both in the torus region and the curved transition to the planar region, the mesh is composed of both quadratic quadrilateral and triangular elements. From experience with the

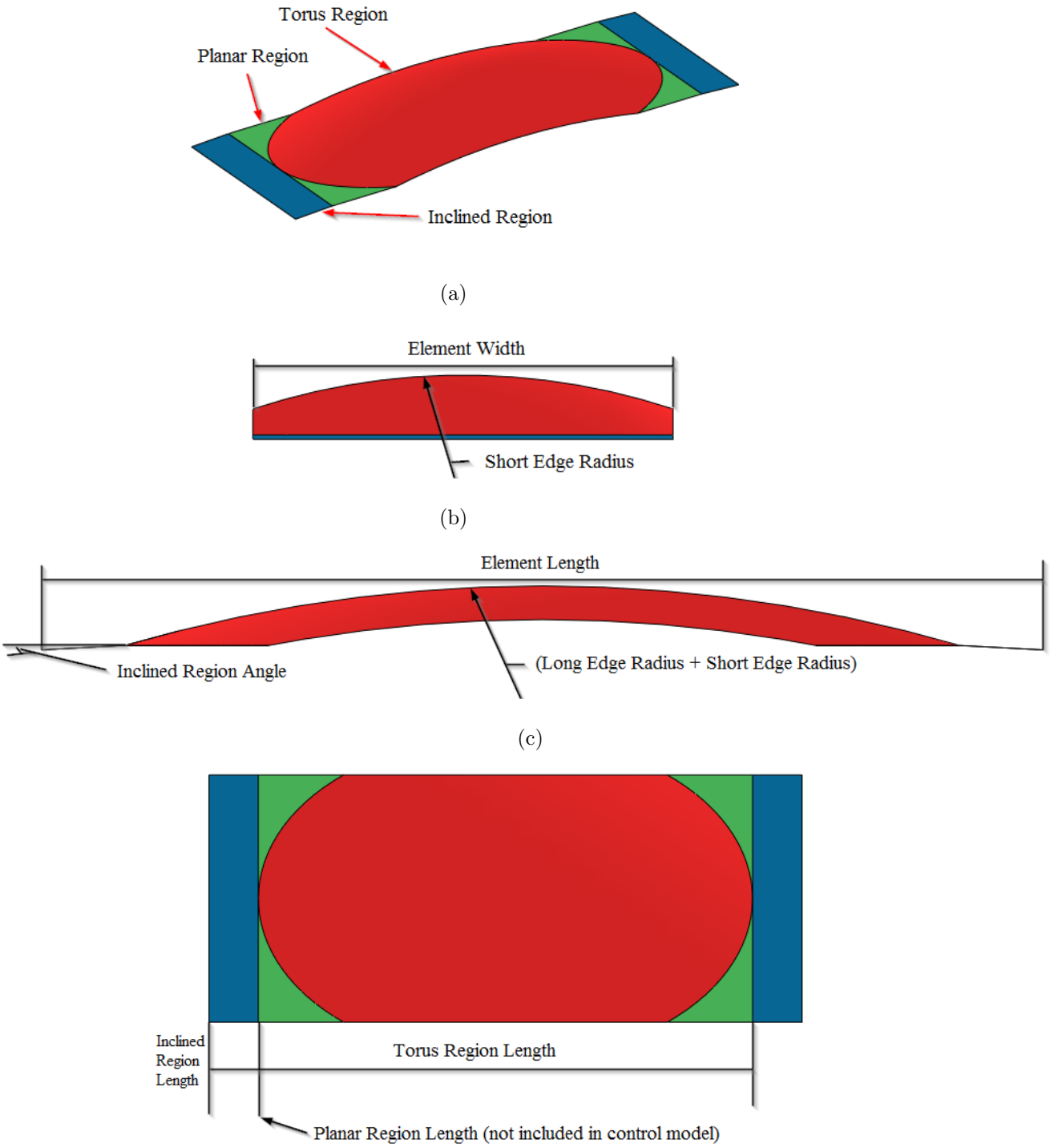

Figure 3.12. (a) Isometric view and (b-d) side views showing regions and parameters.

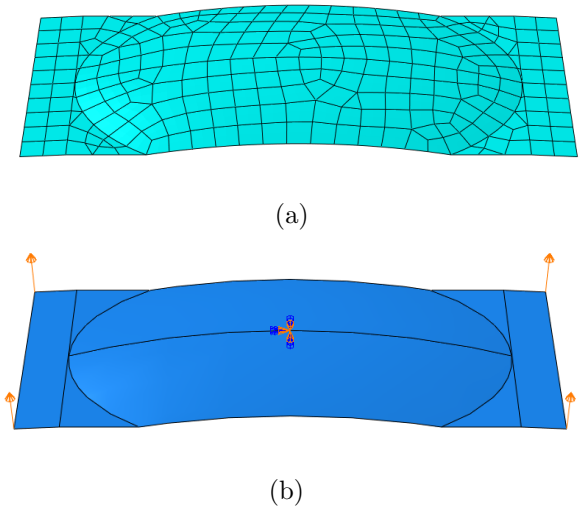

(a)

(b)

Figure 3.13. Pictures of (a) finite element mesh and (b) boundary conditions for control element.

previous element, in which a coarse mesh yielded very similar energy results to a fine mesh, an element size of 5mm is chosen, this results in the mesh shown in Fig. 3.13a.

The analysis took place in three phases to assess the element's stability. These phases were:

1. A perturbation in the negative direction.
2. A load in the snap-through direction.
3. A perturbation in the reverse snap-through direction.

Each phase consists of a loading step, in which the corners are given a specified displacement boundary condition, as shown in Fig. 3.13b and an unloading step, in which the displacement condition is removed and the model is allowed to relax. The center point of the element is completely fixed throughout the analysis to prevent rigid-body motion. A nonlinear, static analysis is chosen due to the large deformations experienced during snap-through. Each step is also given a damping factor of $1 * 10^{-7}$ to facilitate convergence.

After running the analysis, the strain energy for the entire model (ALLSE) was extracted and plotted against the displacement. An example of this plot for the control model is shown in Fig. 3.14. The gap in the plot is the result of boundary conditions forcing the model along an unrealistic energy path following the onset of snap-through. As a result, only the pre-snap and unloading energy paths for the loading phase are shown.

Stability of each individual bi-stable elements is established by the following criteria:

1. If the element returns to its initial state after the load phase, it is monostable.

2. If the element is in a new, stable configuration after the load phase, but returns to the initial configuration after the perturbation phase, it is considered metastable.

3. If the element remains in the new configuration at the end of the analysis, it is bi-stable.

As Fig. 3.14 shows, the control model shows two distinct energy wells and remains in its second state at the end of the analysis, demonstrating that the model is bi-stable. The two configurations of the model from the analysis are given in Fig. 3.15. Comparing Figs. 3.11 and 3.15 shows that the deformed stable state in the analysis closely resembles that of the physical model.

3.2.4 Exploration of Design Space

With the development of the parametric model of the doubly curved element, a script in Python is written to enable the design space exploration by varying the parameters and generating new geometry for several individuals. The steps of the previous analysis are then repeated for each set of input parameters. This section details the results of a parameter study focusing on the aspect ratio of the element and curvature of the torus region. These parameters are the primary driving parameters

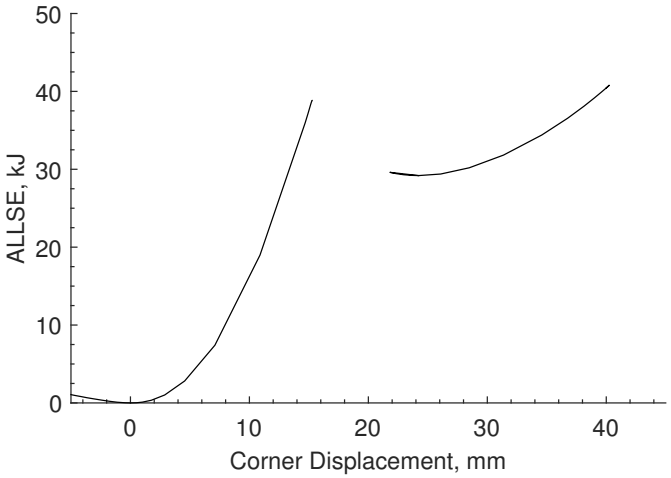

Figure 3.14. Plot of the entire model strain energy versus the displacement of the corner.

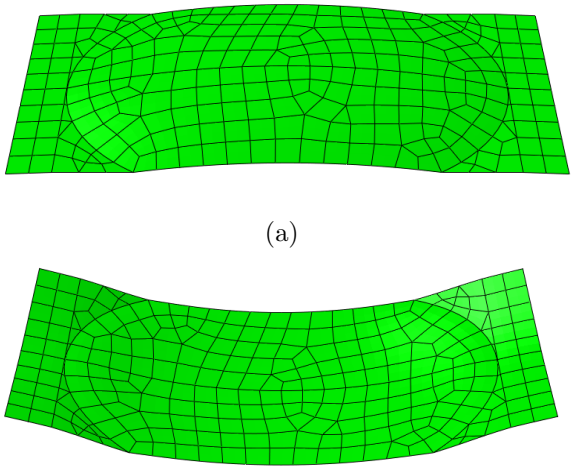

(a)

(b)

Figure 3.15. Results of finite element analysis showing (a) undeformed, stable state and (b) deformed, stable state.

for the bi-stability of the element. A more thorough study investigating the interaction of all the parameters is planned for further development. This section also discusses the embeddability of the element as it relates to the length of the transition regions and the thickness of each region.

Aspect Ratio - Curvature Study

For this study the width and length of the element are varied in increments of 10mm from 40mm to 60mm, and 120mm to 160mm, respectively. The lengths of each region are kept proportional to the control model for this study. At each combination of length and width, the long edge radius of the torus region is varied from 80mm to 220mm, again in increments of 10mm. The minimum short edge radius is chosen so that the arc created by a plane bisecting the element (suggesting the smaller circle of the torus the region derives from, see Fig. 3.9) is less than a half-circle. This is then divided into six equal increments with a maximum radius of 180mm. The values chosen for the radii are based on previous experience in which bi-stability is lost at higher values, where the model becomes closer to a flat plate. At lower values, the curvature becomes exceedingly extreme resulting in new buckling modes to be introduced leading to failure of convergence in the FE analyses.

At each iteration, the ALLSE versus displacement data are extracted and the bi-stability is determined by the previously stated criteria. Figure 3.16 shows the stability data for the study indicating regions of bi-stability by (green) plus sign, metastability by (black) dots and monostability by (red) crosses. At aspect ratios greater than 3.0, there were no stable configurations. The graph shows that there are some additional interactions between width and the other parameters. This is most clearly visible by the reduction in the stable region between $AR = 2.33$ and $AR = 2.4$, which increases again at $AR = 2.5$. The set with $AR = 2.4$ has a 50mm width compared to the 60mm width of the other two. The general trend shows that a long edge radius of around 150mm to 160mm with a short edge radius of 80mm to 100mm is the most favorable curvature, with shorter, wider elements being more favorable for bi-stability.

The design space is explored further by examining the effect of aspect ratio on the specific energy curves, shown in Fig. 3.17. For the aspect ratios greater than 3.0, the energy curves show, as expected, that no stable state was reached after unloading.

Rather, the part, which had snapped-through in the loading step simply followed a smooth curve until it snapped-back, causing the discontinuities in the curves. The shaded part of the plot represents energy surfaces for the two stable states. The graph shows that the 2.33 aspect ratio element has the highest deformed state energy level. The high difference in energy level correlates with the difference in in-plane stiffness of the two stable states [33]. A substantial stiffness difference is desirable for selective stiffness applications, in which the bi-stable elements are used to alter the stiffness of a compliant structure by inducing a change between the available stable states. This comes at the cost of a higher activation energy, also seen in the plot.

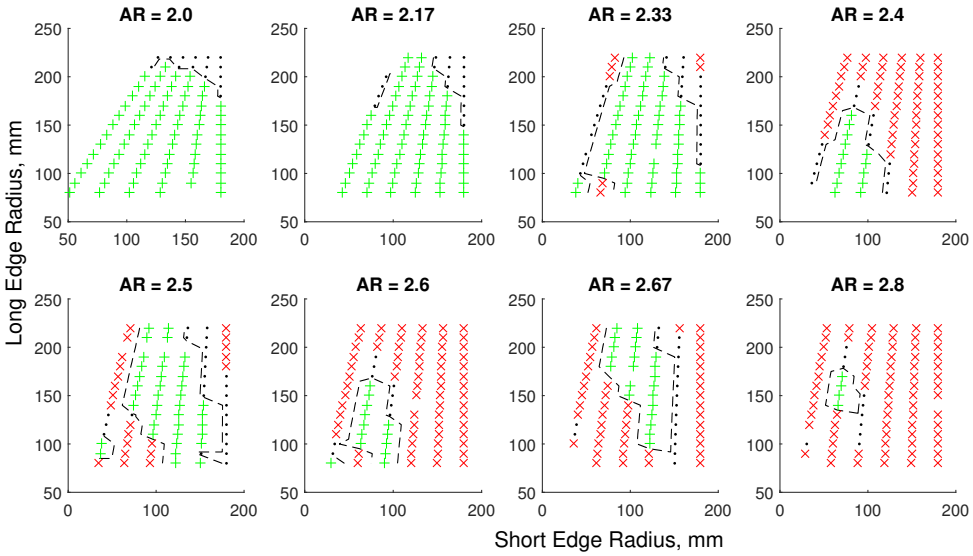

Figure 3.16. Plots of stability at respective curvature and aspect ratio (length/width). The green(+) represents a bi-stable configuration, red(×) is monostable, and black(·) is metastable. The dashed outline is an approximation of the boundary for which the element is bi-stable.

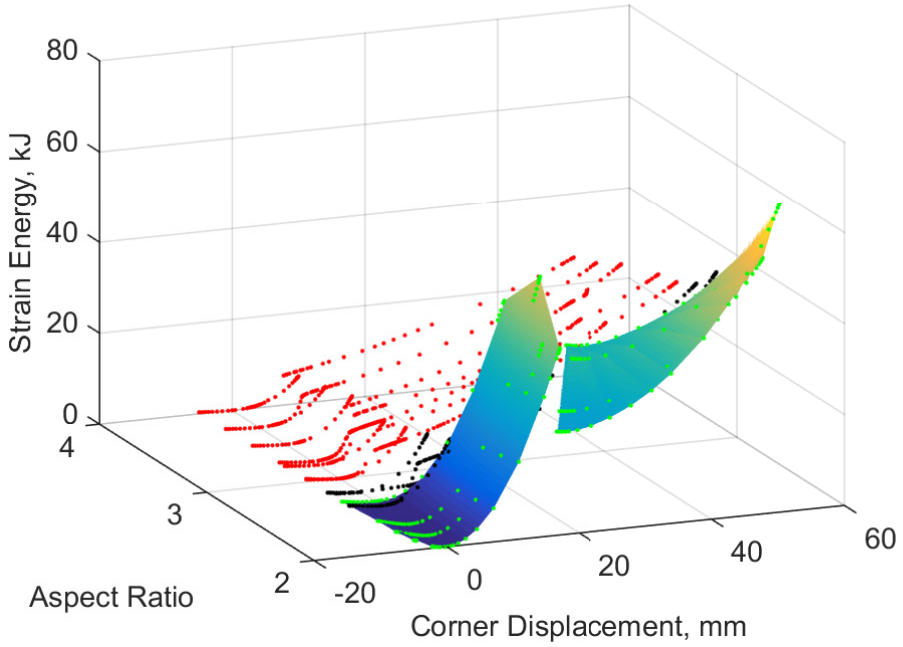

Figure 3.17. Plot of ALLSE versus corner displacement for varying aspect ratios. The shaded region is an interpolation of the surface for each stable state.

Embeddability Study

The embeddability of the element is the ability to constrain it on both edges while retaining bi-stability [33]. Whether or not a given element configuration is indeed embeddable or not requires a separate analysis with different boundary conditions. However, one correlating factor will be the curvature of the short edge in the deformed state. This is gaged in this analysis by measuring the difference in deflection between the middle and the corner of the short edge, shown for example in Fig. 3.18. If this curvature can be minimized, the likelihood that an embeddable element can be achieved will increase. This section describes the effect of the length of the transition regions (planar and inclined) and thicknesses, respectively, on the edge difference.

To study the effect of increasing the transition lengths, the length parameter of the whole model is increased and the difference between that and the control model is

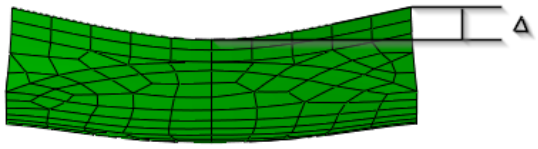

Figure 3.18. Schematic representation of edge difference measurement.

added to first one region, then the other, then split between both. For each iteration, the edge difference is measured. The results of this study are shown in Fig. 3.19. The plot shows a general decrease in the edge difference with increasing length, with the planar region having the greater effect. However, as seen by the lack of contours in the upper right corner of the plot, the element becomes bi-stable. This is expected, as the increasing length also increases the aspect ratio, which was addressed in the last section.

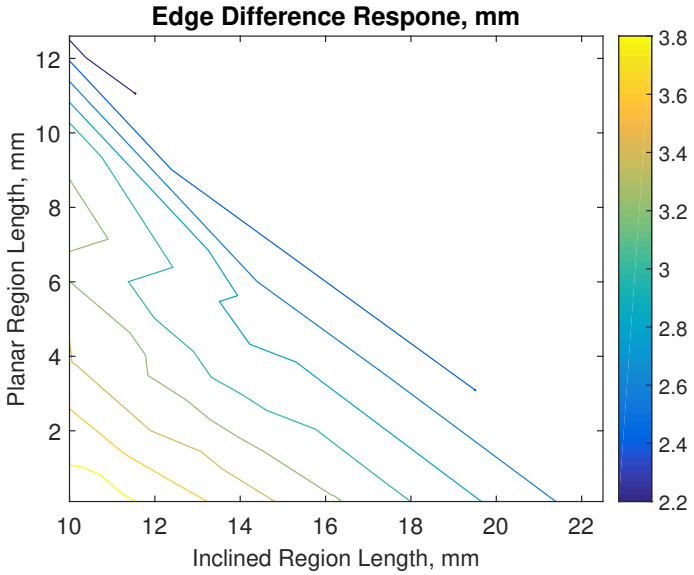

Figure 3.19. Contour plot of edge difference versus length for increasing transition length.

Finally, the effect of thickness in each region is studied by varying it from 0.3mm to 0.5mm by 0.05mm. The data from this analysis are shown in Fig. 3.20. The plots

show a general trend of decreasing edge difference as the inclined region is thickened while the planar region is thinned, with the thickness of the torus region having only a small effect. As with increasing the length of the transition region, however, we also notice that the decreased edge difference appears to correlate with a loss of bi-stability, shown most clearly in the upper left contour plot.

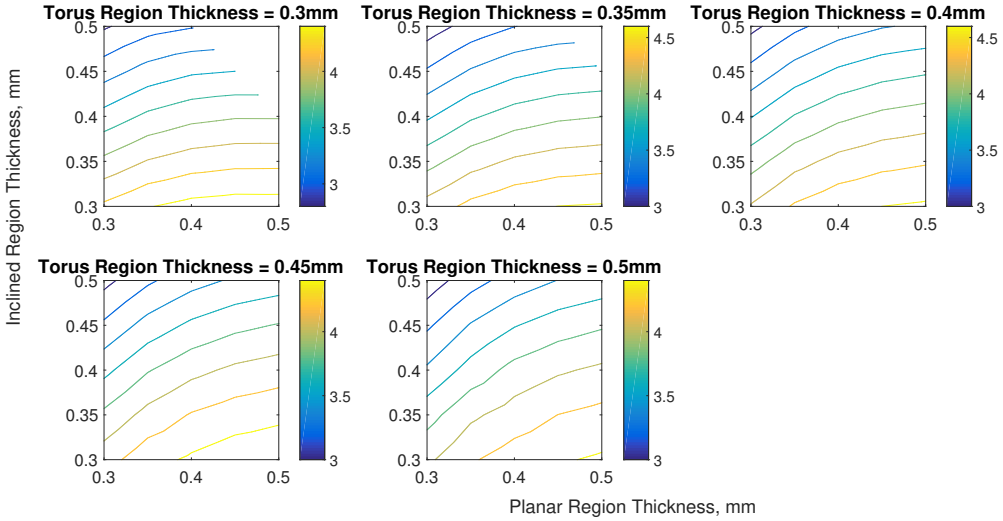

Figure 3.20. Contour plots of edge difference at varying thicknesses.

3.3 Curvature in One Direction with Flexural Reinforcement

The bi-stable element proposed is shown in Fig. 3.21. It is similar in shape to a patented device made from prestressed composites proposed as an aerodynamic surface [34]. The element consists of a curved shell flanked by planar flexural members, both transitioning into an angled region. The curved region acts as an arch. An out-of-plane load on the center of the arch creates in-plane loading in the flexural members. The critical buckling load of the arch forces it into a second state with a snap-through behavior. The energy stored within the arch would cause it to snap back once the load is removed, lacking any boundary conditions to fix it in the second state. However,

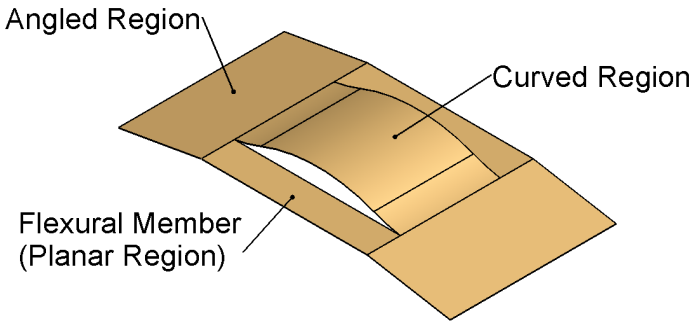

Figure 3.21. Image of bi-stable element with curvature in one-direction with flexural reinforcements denoting main geometric regions.

the load generated in the flexural member counteracts the return force of the curved region. This allows the element to adopt a second stable state. A finite element model is developed showing this snap-through behavior, and a parametric study is conducted to explore the design space of the element.

3.3.1 Finite Element Model

The element is modeled using the Abaqus finite element analysis software. The part is meshed, shown in Fig. 3.22, using a structured mesh consisting of reduced integration, quadratic (S8R) shell elements. The mesh size is set at 2 mm, resulting in a mesh of approximately 800 elements. Previous experience with similar geometries shows that such a mesh is sufficient to determine the element's stability [16]. The material properties used in the model are a Young's Modulus of 3 GPa and a Poisson's Ratio of 0.3. These properties are meant to simulate polylactic acid (PLA), a thermoplastic commonly used in 3D printing. The dimensions of the element, shown schematically in Fig. 3.23 are summarized in Tab. 3.2 as the "control" model. The analysis is completed using Abaqus's nonlinear solver due to the large deformations involved in the snap-through. A small amount of numerical damping is applied, on the

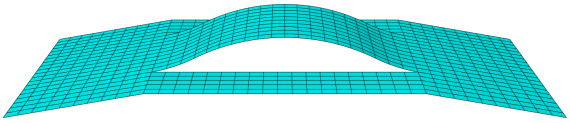

Figure 3.22. Image of bi-stable element mesh.

order of 10^{-7}, as prescribed by the software documentation for this type of buckling problem [35].

The model is held fixed by boundary conditions along the short edges. One side is completely fixed in all degrees of freedom. The other side is allowed to move perpendicular to the edge, but not parallel. The conditions are chosen to emulate embedding the element in a compliant structure which allows in-plane movement, but resists transverse stretching. The center of the curved region is then actuated by a prescribed displacement boundary condition which forces the snap-through behavior. A subsequent analysis step is conducted with the prescribed displacement removed and one support allowed to slide in-plane in order to allow the model to reach equilibrium. Perturbation loads are applied in a similar fashion to each state, both in- and out-of-plane to assess the stiffness and stability of the element, respectively. A schematic representation of these boundary conditions is shown in Fig. 3.24.

3.3.2 Baseline Behavior

Analysis of the control model demonstrates that the element is stable after snapping through. The primary criteria to determine this is by measuring the strain energy stored by the element as the midpoint is displaced vertically. A plot of this data is shown in Fig. 3.25. The curve shows two local minima which indicate stable states. The transition between these states is expressed by an initial buckling on one side of the curved region that rolls across to the opposite side. This behavior is similarly observed in elements using dome-like geometries, and is characteristic of the buckling of curved shells.

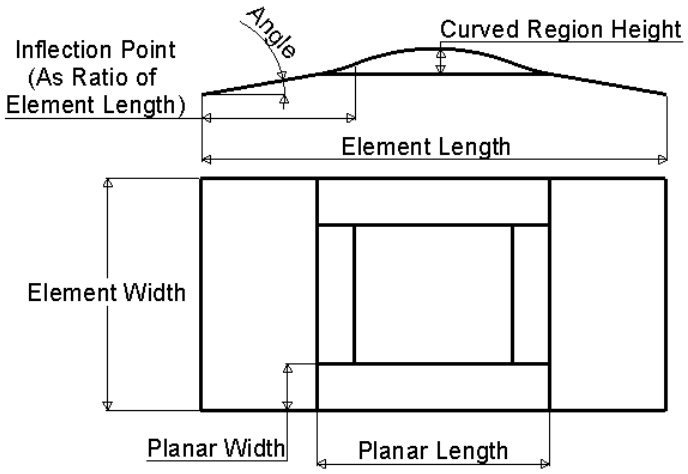

Figure 3.23. Schematic showing parameters varied in study in side view and constant parameters in top view.

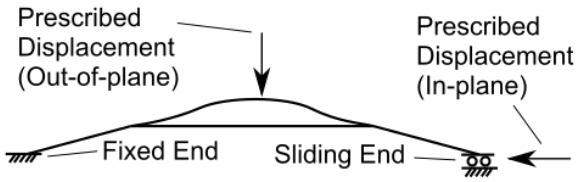

Figure 3.24. Schematic representation of boundary conditions in finite element model.

Another similarity between this element and other bi-stable shells is a curvature induced along the short edge direction in the second state. This curvature prevented clamping on the short edge because doing so resulted in the loss of bi-stability. This hindered previous efforts to embed the element in a structure. The proposed element demonstrates no loss of bi-stability due to the clamped edges, however. The angled regions in this case provide a transition between the curved region and the edge of the element. This allows the proposed element to be embedded in a structure as is without loss of bi-stability.

The stiffness can be calculated by measuring the reaction force to an in-plane perturbation. The results of this analysis are shown in Fig. 3.26. It is clearly demon-

strated in this graph that the stiffness of the element, represented by the slope of the reaction force as the element is compressed, is much higher after the element has been snapped into its second state. Estimating the initial slope, as is demonstrated in the graph, shows that the element has an approximately 3.26 times higher stiffness in the stiff state. This is considerably lower than that observed in bi-stable elements derived from prestressed laminates, but the ease of embeddability and manufacturability suggest that this element warrants further investigation.

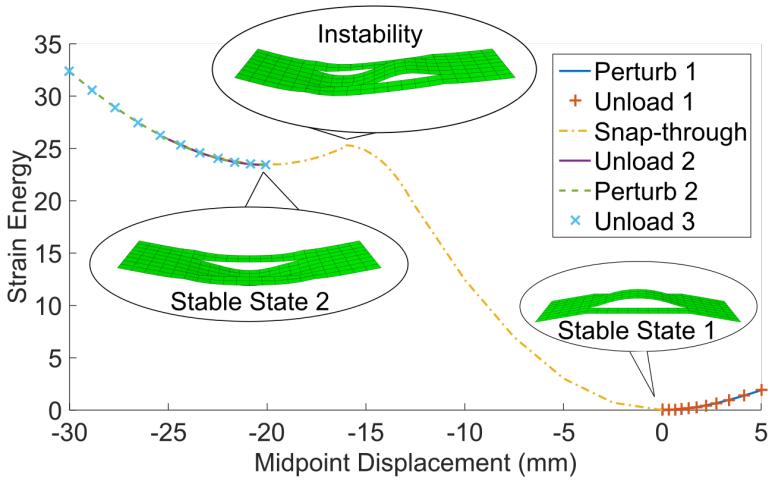

Figure 3.25. Plot of strain energy versus displacement of control model showing deformed state at snap-through instability and both stable states.

3.3.3 Parametric Study Results

A parametric study is conducted to explore the design space of the element. The four dimensions shown in the side view of Fig. 3.23 are chosen for the initial study. These parameters have the greatest impact on placement of the element within the rib structure, and therefore represent a geometric constraint on embeddability. Each parameter is varied independently through a range of values shown in Tab. 3.2. For each configuration, the stability and stiffness is assessed as previously described.

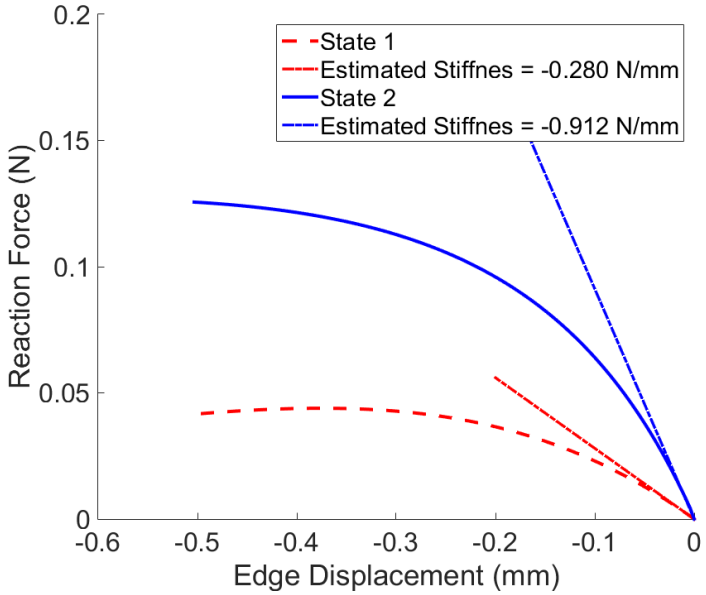

Figure 3.26. Plot of reaction force to compressive displacement in-plane for control model.

Element Length.

The stability of the element is decreased as the element length is increased. This is shown in Fig. 3.27(a) by the lower difference in energy between the second state and the instability. The in-plane response of the element is shown in Fig. 3.28. Figure 3.28(a) shows that the stiffness generally decreases as the element gets longer, as the angled region produces a larger moment arm. The far end of the parameter sweep reveals that the element becomes more prone to buckling. Figure 3.28(b) shows, however, that the stiffness of the undeformed state (State 1) decreases much more rapidly, resulting in a stiffness difference between the states that increases with the square of the length. This parameter sweep demonstrates a trade-off between the desired traits of high stiffness for a structural member and the difference in stiffness between states necessary for meaningful selective stiffness.

Table 3.2. Parameters used in parametric study of flexurally-reinforced element (parameters with only control value listed not explored in this study).

Parameter	Control	Minimum	Maximum
Element Length	75 mm	75 mm	110 mm
Inflection Point Ratio	0.33	0.3	0.4
Curve Height	5 mm	5 mm	7.5 mm
Angle	10°	0°	10°
Planar Length	37.5 mm	(Varies as 0.5 times element length)	
Element Width	40mm		
Planar Width	10 mm		
Element Thickness	0.5 mm		

Inflection Point Ratio.

Varying the location of the inflection point along the length of the element increases the curvature of the curved region. This causes a slight decrease in the activation energy of the snap-through, seen in Fig. 3.27(c). However, a simultaneous decrease in the energy of the second stable state results in no real change in stability. The in-plane stiffness of the element is not largely affected by this parameter, however, as Fig. 3.29 shows. The reaction force plot shows little to no effect on State 1 as the parameter is varied. The response of State 2 shows an almost periodic behavior, but with no significant change in initial stiffness. This is supported by Fig. 3.29(b). Although the stiffness difference exhibits a general increase with the increased curvature, the range of values is relatively small.

Curve Height.

Increasing the height of the curved region causes a significant increase in the activation energy of the element. This effect is shown in Fig. 3.27(b). The increase is a result of a higher force necessary to begin buckling the arch formed by the curved region. The curve height, like the location of the inflection point, shows little effect on the response of State 1. However, it has a significant impact on the stiffness of the deformed state. Figure 3.30(a) shows that the stiffness of State 2 noticeably decreases with increasing height. The two states have nearly the same stiffness at approximately 7mm, as seen in Fig. 3.30(b). State 2 then becomes more flexible than state 1 at larger curve heights. However, the difference is still relatively small. This property is nonetheless significant for tailoring the structural properties of a network of such embedded elements.

Angle.

The stiffness behavior noted previously is far more pronounced as the angle of the element is varied. The flat plate element naturally has an incredibly high in-plane stiffness in the undeformed state, but also the most pronounced buckling behavior. Snapping the element into the deformed state then induces an angle in the plate, which drastically reduces the in-plane stiffness, as the inset in Fig. 3.31(a) shows. Figure 3.31(b) shows a distinct trend of increasing stiffness ratio, with the element switching from stiff/flexible to flexible/stiff in State 1 and 2, respectively, at approximately 6°. The stability of the element is largely unaffected by the angle, as demonstrated in Fig. 3.27(d).

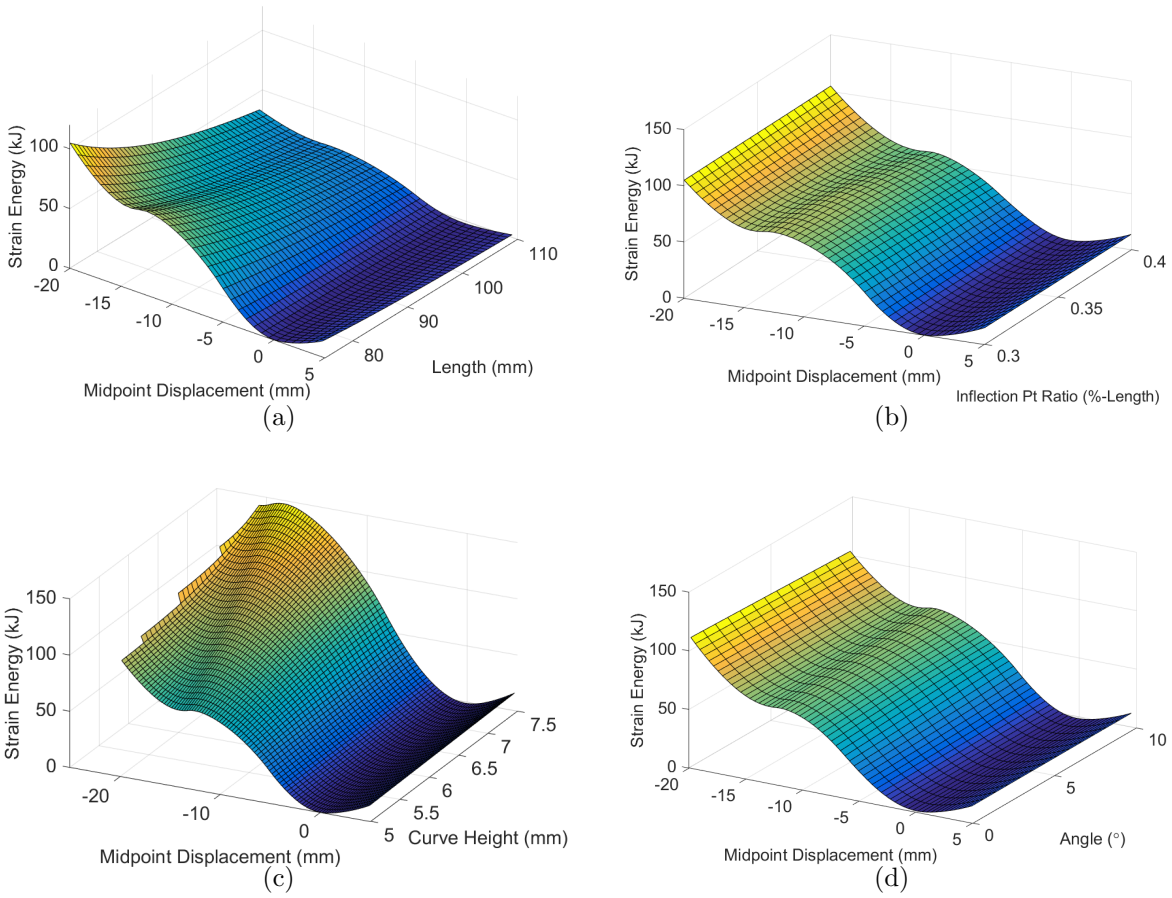

Figure 3.27. Strain energy versus displacement plots for isolated slit-plate bi-stable elements varied by a) length, b) inflection point ratio, c) height, d) angle.

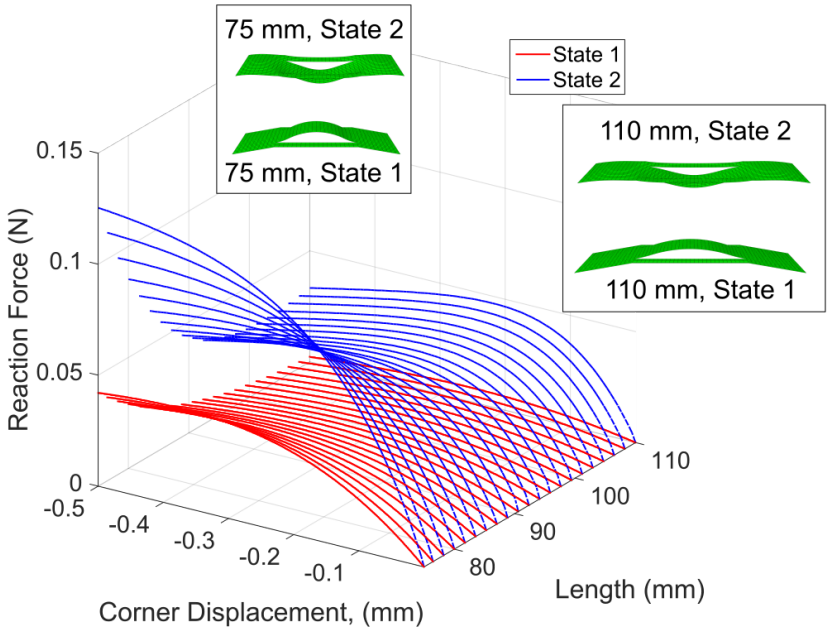

(a)

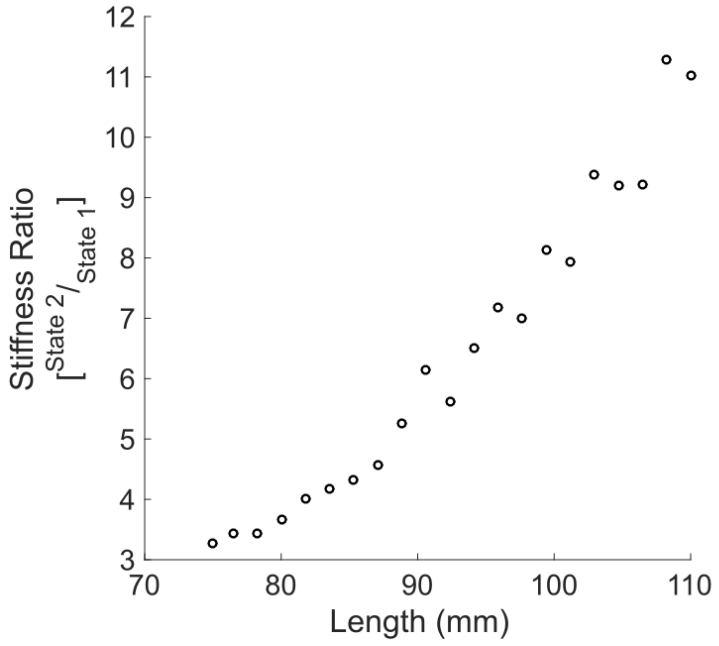

(b)

Figure 3.28. In-plane stiffness response varied by element length.

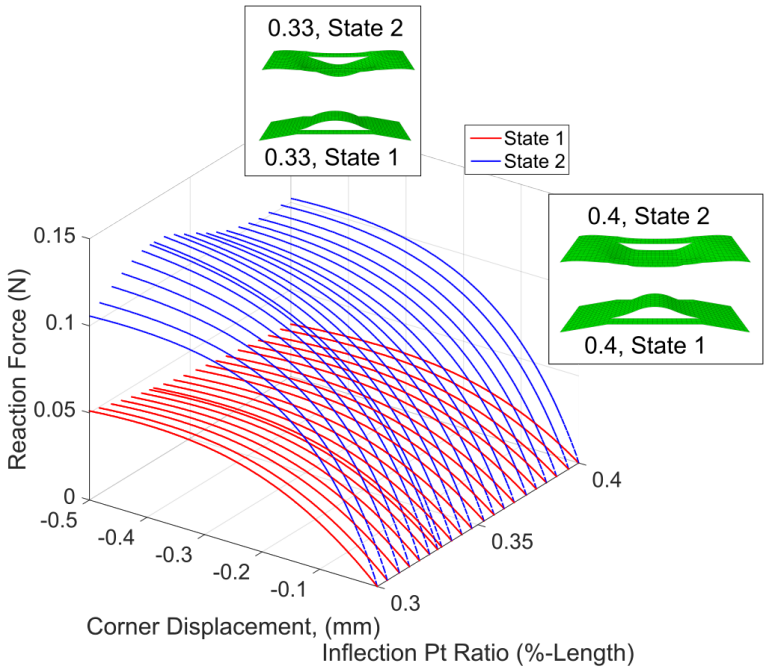

(a)

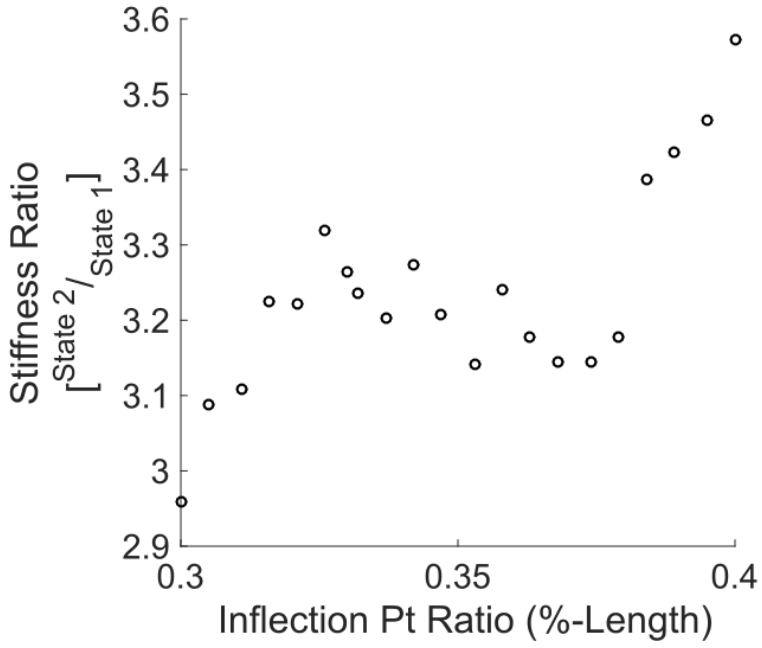

(b)

Figure 3.29. In-plane stiffness response varied by location of inflection point as a ratio of element length.

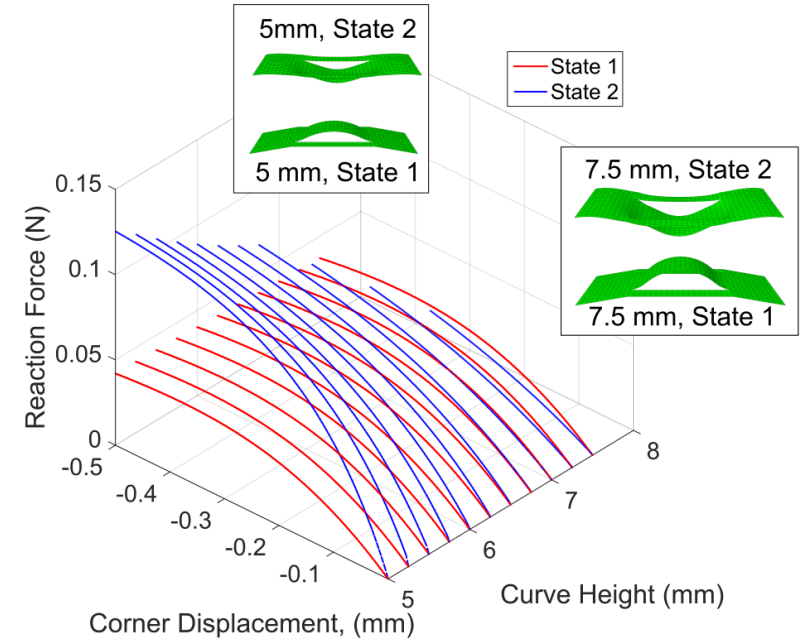

(a)

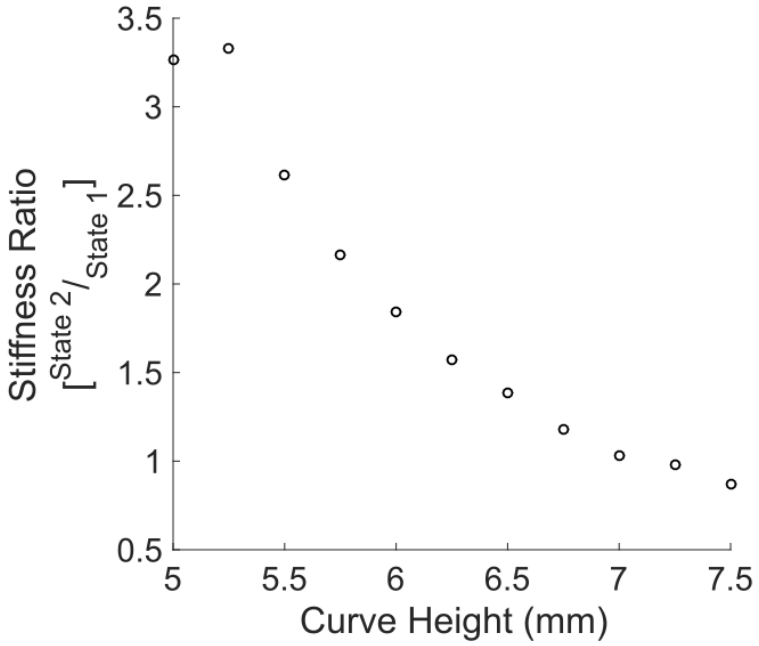

(b)

Figure 3.30. In-plane stiffness response varied by height of curved region.

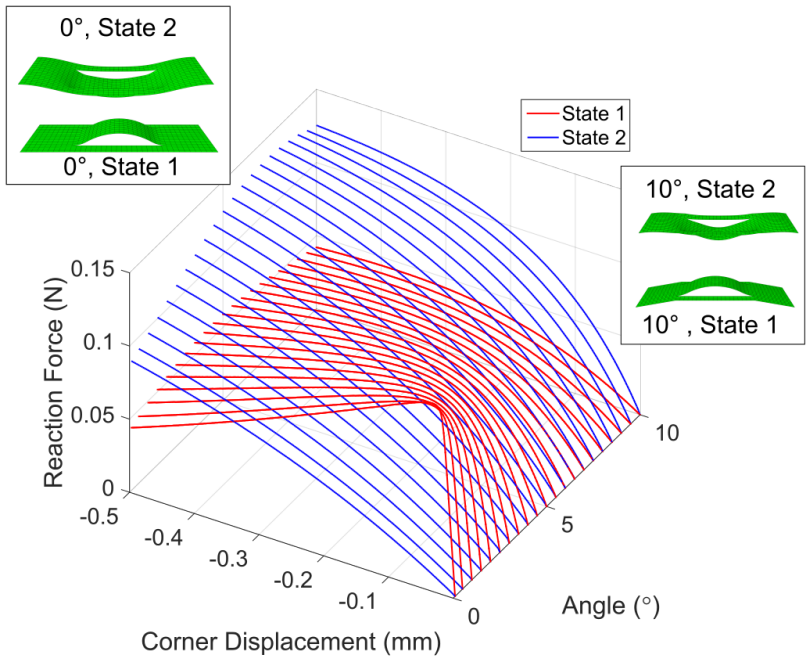

(a)

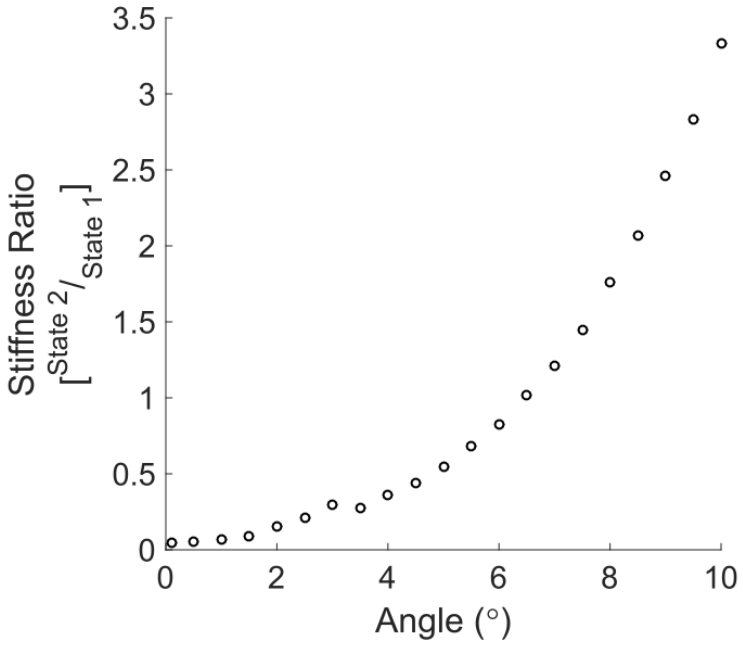

(b)

Figure 3.31. In-plane stiffness response varied by element angle.

4. MORPHING AIRFOIL DESIGN WITH LOCAL SELECTIVE STIFFNESS

Sections of this chapter are based on the conference contribution selected for publication at the time of writing:
D. M. Boston, A. F. Arrieta, J Rivas-Padilla: "Monolithic morphing rib with selective stiffness from embeddable bi-stable elements". In Proceedings of the ASME 2018 Conference on Smart Materials, Adaptive Structures and Intelligent Systems, SMASIS 2018, American Society of Mechanical Engineers. 2018.

Past work on using local selectively stiff elements for compliant airfoils yielded an optimized design for that type of element [36]. A simplified design was instead chosen for an initial analysis of the new embedded element discussed in the previous chapter. This design mimicked earlier testing efforts (see Fig. 2.8) and allowed greater flexibility for the large out-of-plane deformation the element experiences during snap-through. This initial study is described below.

This effort was followed by a design optimization to determine the best configuration of element location and element parameters for this simple box-like design. A fully optimal design was not required, as it is only meant to demonstrate the viability of the selectively stiff bistable element embedded in an airfoil. A response surface methodology was thus chosen for simplicity to produce a design. The process for this optimization technique and the resulting design is presented in this chapter. This is followed in the next chapter by a discussion of the manufacturing and testing of the final rib design.

4.1 Initial Model Embeddability Study

Having proven the feasibility of the bi-stable element as a selectively stiff structural member, an analysis is conducted on an element embedded in an airfoil with a truss-like structure. A NACA0014 profile is selected for the airfoil. A chord length of 200mm is chosen for the sake of manufacturability using the limited build volume of a hobbyist 3D printer. The rib is composed of a rigid D-spar at the leading edge. The bi-stable element connects diagonally across the rib from the central spar. A rear spar forms a wing box with the rear edge of the bi-stable element. A model of the rib is shown in Fig. 4.1. A finite element model is also developed for the rib, and a parametric study similar to that described in the previous chapter is conducted to determine the structural impact of the bi-stable member.

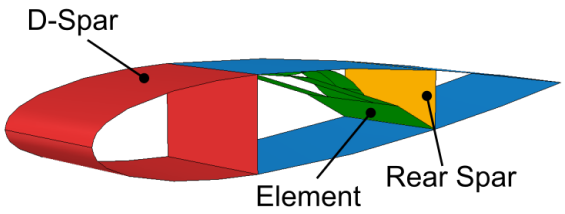

Figure 4.1. Image of rib with embedded bi-stable element.

4.1.1 Finite Element Analysis

The element embedded in the rib is meshed using the same parameters discussed in Section 3.3.1. The rest of the rib structure is expected to undergo smaller deformations relative to the element and requires lower fidelity. A linear mesh is therefore used for the rib to reduce the computational cost of the model. The mesh is shown in Fig. 4.2. The analysis is carried out in the same manner as the isolated element, with nonlinear, static steps that use a small damping factor. The D-spar of the rib

is held fixed at the edges throughout the analysis. Snapping loads are applied to the element in a local coordinate system matching the isolated model. Perturbation loads, shown in Fig. 4.3 are applied to the airfoil in the form of a quasi-static aerodynamic load derived from the pressure coefficient distribution of a NACA0014 airfoil traveling 20 m/s at a 5° angle of attack.

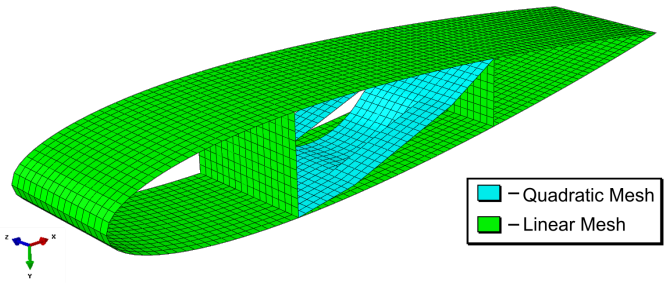

Figure 4.2. Image of rib mesh (underside) showing regions with quadratic and linear elements.

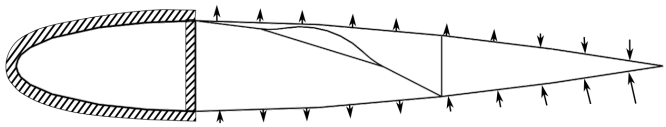

Figure 4.3. Schematic representation of rib boundary conditions for perturbation loads. D-Spar remains fixed as shown throughout analysis.

The strain energy-displacement plots derived from the analysis are shown in Fig. 4.4. The trends shown for each parameter sweep match those of the isolated element shown in the previous chapter (see Fig. 3.27). The most significant change is a loss of bi-stability at the edges of the parameter range. This is illustrated in Fig. 4.5 which shows the trailing edge (T.E.) deflection resulting from the simulated aerodynamic load in each state of the element. The mono-stable configurations occur solely at the beginning or end of the range, demonstrating a stability boundary for that parameter. The response of the bi-stable configurations, however, shows a similar pattern

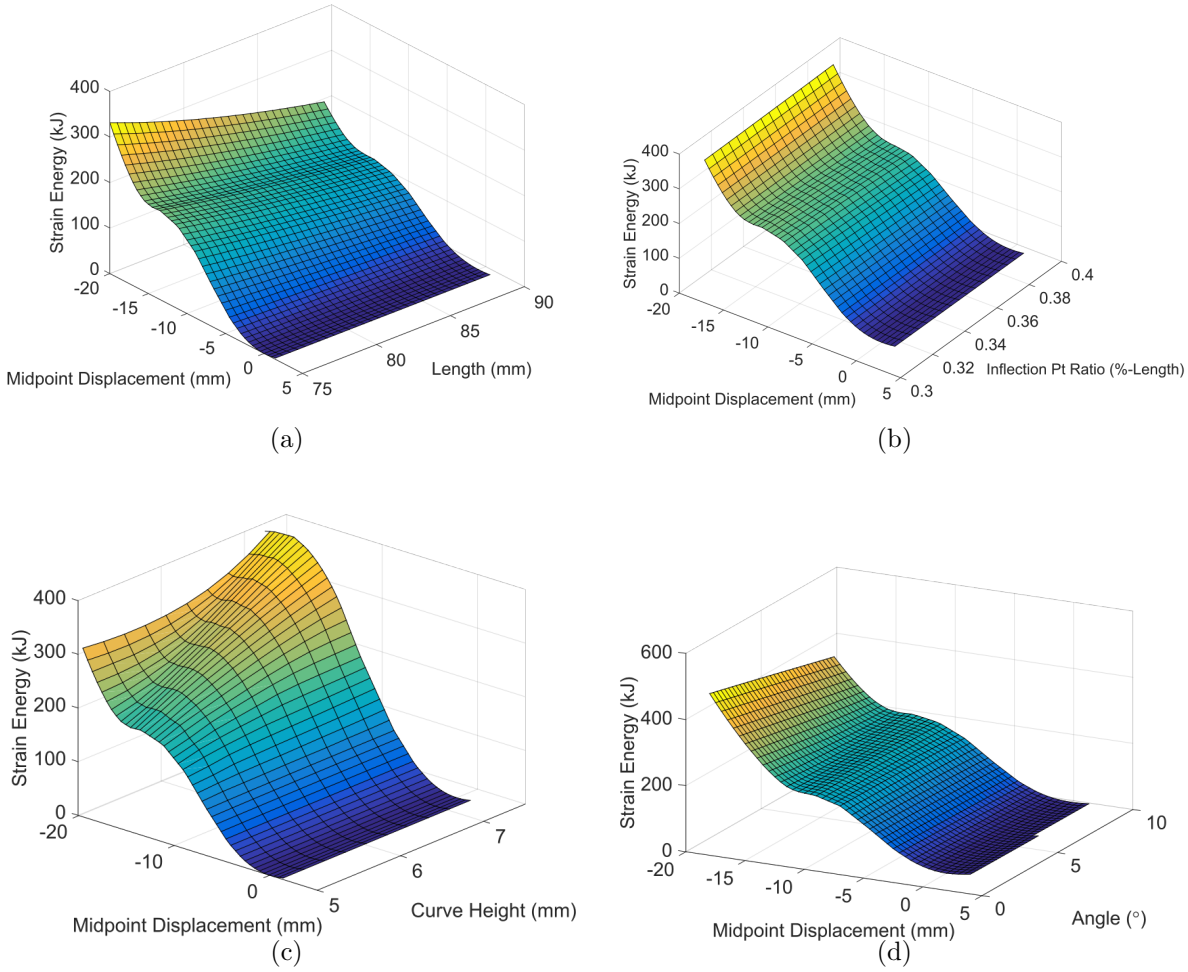

Figure 4.4. Strain energy versus displacement plots for embedded elements varied by (a) length, b) inflection point ratio, c) height, d) angle.

as well. The rib structure decreases in stiffness with increasing element length, but the difference in response resulting from stiffness difference increases. Varying the inflection point results in no significant change in stiffness. The curve height still has a significant effect on the activation energy of the snap-through. Additionally, the switching behavior from flexible/stiff to stiff/flexible observed by varying the curve height or angle is seen in the deflection of the T.E. of the rib with the embedded element.

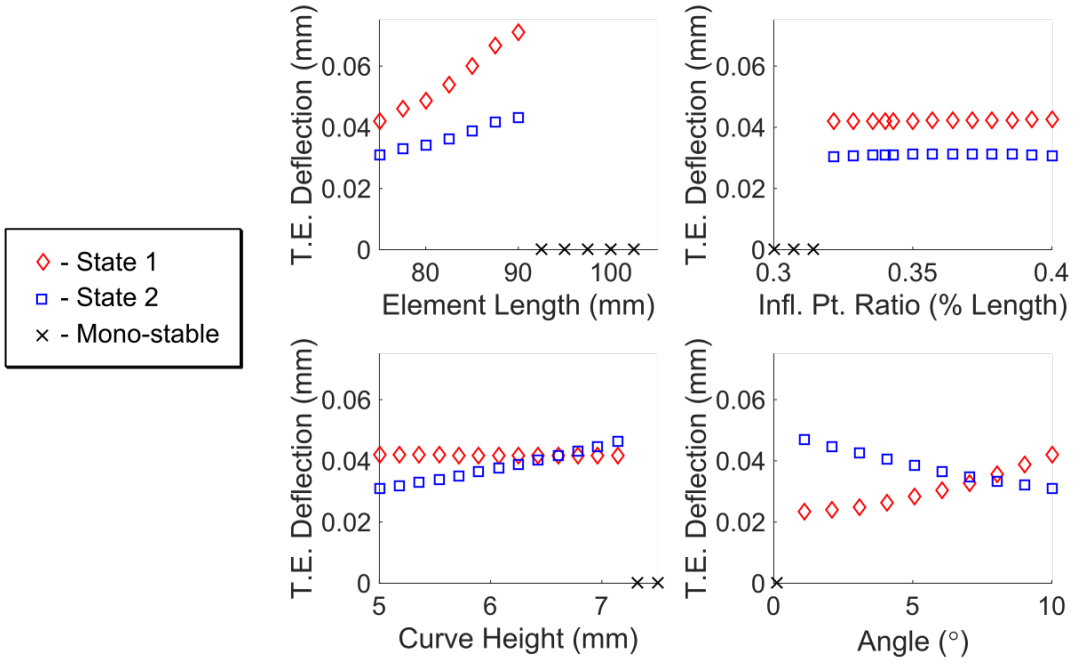

Figure 4.5. Vertical trailing edge deflection of rib in response to perturbation load at each element state. Monostable configurations not evaluated for stiffness.

These results suggest that the element acts as a truss-like element in the rib structure, preserving the trends in stiffness properties for each state. The loss of stability at the edges of the range indicate some effect from embedding the element, however minor. An optimized airfoil design therefore is determined with the element embedded, at least initially, to ensure this effect is accounted for.

4.2 Final Design

An optimization employing a response surface methodology and sequential quadratic programming algorithm were used to produce a selectively stiff airfoil design. Figure 4.6 shows a schematic representation of the process used in the optimization. The details of this process are given in this section. A model is first developed, then analyzed at a series of design points according to an experimental design. This allows an approximate model of the T.E. deflection and element stability to be developed as a response surface. The approximation can then be used to find an optimal design point. This last is an iterative process, in which the inputs of the response surface affect the outcome of the optimization and must therefore be tuned to provide a realistic simulation.

4.2.1 Model Description

The final parametric model used in the optimization is shown in Fig. 4.7. Notable changes to this model are the addition of parameters for offsetting the element in the y-direction, the addition of a spring element, and an increase in chord length to 250 mm. The extra degrees of freedom in the placement of the model allow the stiffness difference to be used more effectively. The addition of the spring element is in response to an aeroelastic analysis of the initial rib design that demonstrated that a continuous skin is too stiff to allow meaningful deflections and results in localized buckling, which is aerodynamically undesirable [37]. This is supported by the previous work in this area, which includes a section of corrugated skin that possesses a high bending stiffness

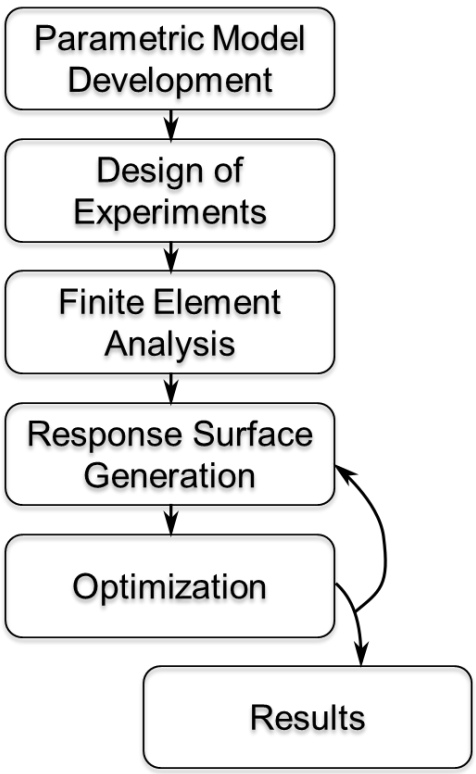

Figure 4.6. Flow chart of optimization.

and a low axial stiffness [36]. A total of 20 parameters are thus identified, including: element geometry, element location, spring location and properties, thicknesses of each region, and material properties of the rib and element, respectively. The rib is modeled in Abaqus using the same techniques described in Section 4.1.1.

4.2.2 Response Surface Methodology

A response surface is a statistical tool used to approximate complex systems [38]. It assumes a given measured quantity is a function of a series of input variables, or:

$$y = f(\mathbf{x}) + \epsilon \tag{4.1}$$

where y is the response, $\mathbf{x}$ is a vector containing the input variables, and ϵ is the error (for a deterministic model such as this, $\epsilon = 0$). Data of the response at various levels

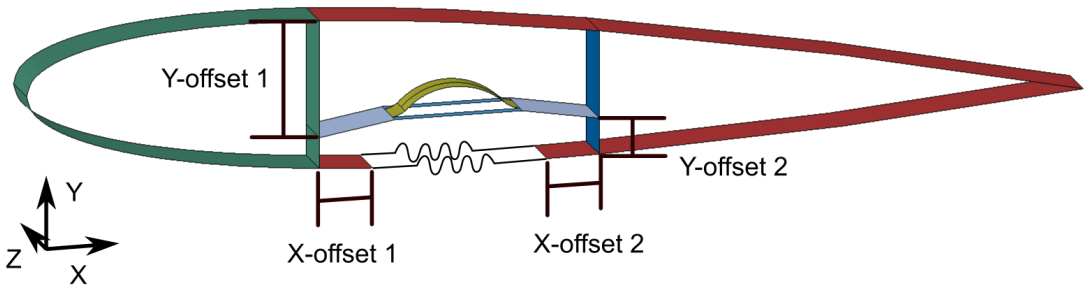

Figure 4.7. Parametric rib model used for optimization. Colored sections indicate regions of varying thickness. Parameters for element geometry shown previously in Chapter 3.

of input is collected and it is fit to a model. The simplest model for the purposes of optimization is a second order polynomial model of the form

$$f(\mathbf{x}) = \beta_0 + \sum_{i=1}^{k} \beta_i x_i + \sum_{i=1}^{k} \sum_{j=i}^{k} \beta_{ij} x_i x_j \tag{4.2}$$

where k is the number of parameters in the model and β are a series of unknown constants. The constants are determined by forming a linear system of equations with the constants as variables and the inputs as coefficients. So, for n measured input/response sets, the system is

$$\begin{bmatrix} 1 & x_{1,1} & x_{2,1} & \cdots & x_{k,1} & x_{1,1}x_{1,1} & x_{1,1}x_{2,1} & \cdots & x_{k,1}x_{k-1,1} & x_{k,1}x_{k,1} \\ 1 & x_{1,2} & x_{2,2} & \cdots & x_{k,2} & x_{1,2}x_{1,2} & x_{1,2}x_{2,2} & \cdots & x_{k,2}x_{k-1,2} & x_{k,2}x_{k,2} \\ \vdots & \vdots & \vdots & & \vdots & \vdots & \vdots & & \vdots & \vdots \\ 1 & x_{1,n} & x_{2,n} & \cdots & x_{k,n} & x_{1,n}x_{1,n} & x_{1,n}x_{2,n} & \cdots & x_{k,n}x_{k-1,n} & x_{k,n}x_{k,n} \end{bmatrix} \begin{bmatrix} \beta_0 \\ \beta_1 \\ \vdots \\ \beta_{\frac{(k+1)(k+2)}{2}} \end{bmatrix} = \begin{bmatrix} y_1 \\ y_2 \\ \vdots \\ y_n \end{bmatrix} \tag{4.3}$$

This is then generally solved using the least squares method. The minimum number of data points required to use this method, as Eq. (4.3) suggests, is $\frac{(k+1)(k+2)}{2}$. There are a number of experimental designs, however, that use additional data points to increase the accuracy of the model, such as full-factorial and Box-Behnken designs. The number of experimental trials required by these designs tends to increase

exponentially with the number of parameters in the model. This quickly becomes impractical or impossible for large numbers of parameters, so sub-optimal designs are instead utilized. Such an experimental design was created for this study using the JMP statistical software containing 1,000 design points using three possible levels for each design variable. Naturally, not every combination of the three levels was represented, as this would be a full-factorial design.

The experimental design was analyzed twice for different upper and lower levels of the design variables. This yielded a total pool of 2,000 possible designs to evaluate. Each design was analyzed in Abaqus as previously described. The displacements of the T.E. at each state, the energy at the second stable state, and the activation energy of the snap-through were measured at the end of each analysis. These were initially used to calculate a fitness function (discussed in the next section), which was then modeled as a response surface, an example of which is shown in Fig. 4.8. The figure shows the difficulty in visualizing the function and assessing its validity. This approach ultimately proved to be inaccurate, as will be discussed later. Instead, the specific outputs, displacement at the first state, stable energy of the second state, etc., were modeled individually.

Response Surface Validation

Two methods for assessing the accuracy of a response surface are calculating the R-squared value and the "Leave-One-Out" method. The latter method involves recomputing the constants of the response surface while excluding a design point. The real value of this excluded point is then compared to that computed by the new approximation. The difference of these values forms an error which can be averaged over the entire set of design points used to create the original response surface.

Using this method results in errors of 0.0022 mm and 0.0192 mm for the State 1 and State 2 T.E. deflections, respectively, with typical deflections on the order of $10^{-}1$ mm and 10^{0} mm. The R-squared values for these surfaces are also $R^2 = 0.8951$

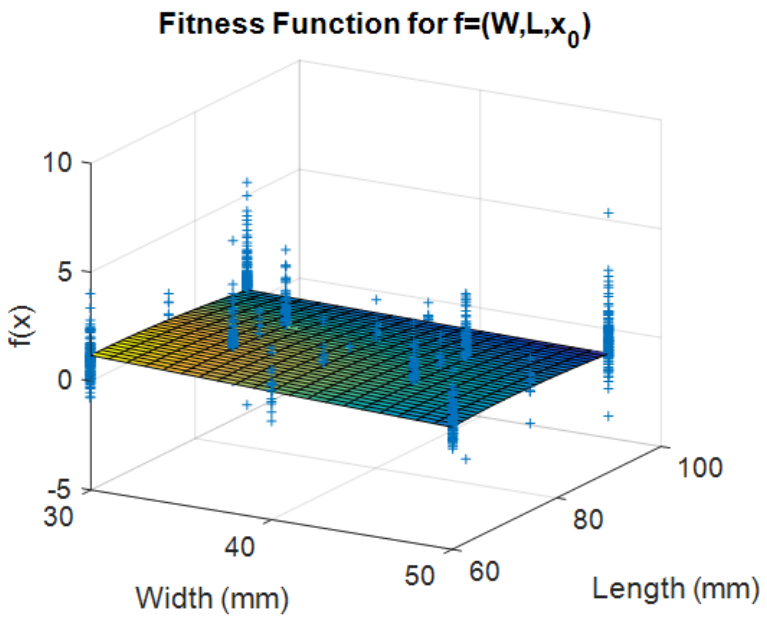

Figure 4.8. Plot of response surface calculated for a range of widths and lengths with all other parameters held constant compared to fitness function values (+).

and $R^2 = 0.7092$. These values indicate that, especially for the State 2 response, the response surfaces calculated are rough approximations at best. The energy response surfaces proved to be highly inaccurate, likely because of significant variation from design to design. This suggests that a quadratic response surface is unsuitable to capture the behavior of the energy. It also suggests that there are significant interactions between the parameters not captured in the previous parameter studies, which generally indicated smooth behaviors within a single parameter. These response surfaces were therefore excluded from the final optimization

4.2.3 Optimization

The ultimate goal of optimizing the airfoil with the embedded element is to produce a design that adequately demonstrates the selectively stiff principle. To this end, a series of optimization objectives is established:

1. Maximize stiffness difference

2. Minimize tip deflection in rigid state

3. Maximize difference between activation energy and stable energy of second state

The last objective could not be accounted for, unfortunately, due to the difficulties with obtaining a satisfactorily accurate energy response surface. The final result was instead modeled again in Abaqus to ensure bi-stability and small modifications were made of single parameters as necessary based on knowledge gained from the parameter studies.

Problem Formulation

The above objectives were interpreted into a series of mathematical statements. These were then developed into a fitness function for use in the following optimization problem formulation:

Minimize:

$$f(\mathbf{x}) = \frac{|d_{rigid}|}{|d_{flex}|} + \frac{1}{4}|d_{rigid}|$$

Subject to:

Parameter	Limit	Parameter	Limit
Width	$30mm \leq W \leq 50mm$	Angled Region Thickness	$0.5mm \leq a_{th} \leq 1mm$
Length	$60mm \leq L \leq 90mm$	Planar Region Thickness	$0.5mm \leq p_{th} \leq 1mm$
Planar Region Length	$0.3 \leq \frac{L_p}{L} \leq 0.89$	Curved Region Thickness	$0.5mm \leq c_{th} \leq 1mm$
Angle	$0.1° \leq \theta_{el} \leq 15°$	Y-offset 1	$0 \leq y_1 \leq 1$
Planar Region Width	$5mm \leq W_p \leq 20mm$	Y-offset 2	$0 \leq y_1 \leq 1$
Curve Height	$4mm \leq h_{el} \leq 7mm$	X-offset 1	$0 \leq x_1 \leq 1$
Inflection Point Ratio	$0.3 \leq infl \leq 0.5$	X-offset 2	$0 \leq x_2 \leq 1$
D-spar Thickness	$0.5mm \leq D_{th} \leq 2mm$	Spring Constant	$3\frac{N}{mm} \leq k \leq 12\frac{N}{mm}$
Bounding Spar Thickness	$0.5mm \leq b_{th} \leq 2mm$	Material 1 Young's Modulus	$900MPa \leq E_1 \leq 3000MPa$
Airfoil Thickness	$0.5mm \leq airf_{th} \leq 2mm$	Material 2 Young's Modulus	$900MPa \leq E_2 \leq 3000MPa$

The terms in the fitness function, d_{rigid} and d_{flex} represent the T.E. deflection measured in each state when applying the simulated aerodynamic load. The behavior in one state has the potential to switch between rigid and flexible when compared to the other state, as observed in the parameter studies (see Section 3.3.3). The deflection of each state is therefore pre-determined. The higher value is assigned to d_{flex}, and the lower value to d_{rigid}. The fitness function uses a weight penalty of $\frac{1}{4}$ on the second term, as this represents the second objective, which is of lesser concern and generally operates on a larger scale than the deflection comparison. Each of the design parameter constraints is chosen based on physical limits, practical limits derived from the parametric studies, or, in the case of thickness, limits of the manufacturing process.

Optimization Methodology

The optimization was carried out using the fmincon function of the MATLAB computational software. This function is meant to handle nonlinear, smooth functions and nonlinear constraints. It was initially chosen in order to handle a nonlinear constraint provided by energy response, essentially verifying the bi-stability of the optimized configuration. It was carried through after the energy response surfaces were discarded. The function uses a number of different solver algorithms. The algorithm chosen for this problem was 'SQP' or Sequential Quadratic Programming. This is a fast and accurate solver for nonlinear problems [39].

The general process for SQP is to use a Quasi-Newton method to form a quadratic programming sub-problem. The solution of this problem results in a search direction for the optimizer. A line search method is then employed in which various steps are taken in the search direction to reduce the value of the objective function. This is accomplished by forming a penalty function with the objective function and all constraints, with a suitably large penalty assigned to constrains that are violated. The SQP algorithm is therefore particularly robust when using bounds, as seen in this problem. The process is repeated until the Karush-Kuhn-Tucker conditions are satisfied, or a set of tolerances has been met that indicate the solution is at least a local minimum. A set of 33 initial design points were given to the optimizer to ensure the local minimum calculated by the solver is actually a global optimum of the design space. The set consisted of a known feasible design, both upper and lower bounds, and thirty pseudo-random designs within the design space.

4.2.4 Results

The geometry of the final design produced by the optimizer is shown in Fig. 4.9. The corresponding thickness and material properties are provided in Table 4.1. Analyzing this design in Abaqus shows that the element will snap-through to a second stable state, shown in Fig. 4.10. The T.E. deflections are 0.546 mm and 0.087 mm

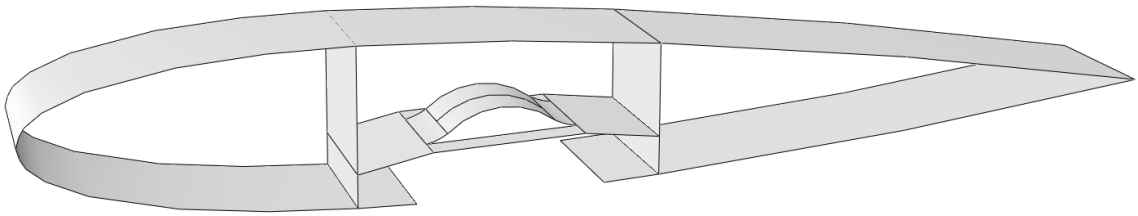

Figure 4.9. Optimized selectively stiff airfoil geometry (spring not pictured).

in States 1 and 2, respectively. This represents a 6.28 ratio of stiffness difference, compared to a maximum of approximately 2 previously observed in the initial study. This increase in difference is largely due to more efficient placement of the element between the two spars.

Table 4.1. Optimized properties for the selectively stiff airfoil.

Parameter	Value
D-spar Thickness	1.147mm
Bounding Spar Thickness	1.046mm
Airfoil Thickness	1.008mm
Angled Region Thickness	0.831mm
Planar Region Thickness	0.878mm
Curved Region Thickness	0.698mm
Spring Constant	$8.272\frac{N}{mm}$
Material 1 Young's Modulus	1669MPa
Material 2 Young's Modulus	2594MPa

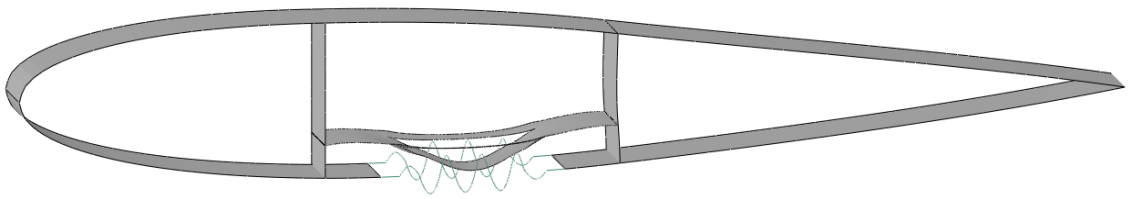

Figure 4.10. Airfoil with element in second stable state.

5. SELECTIVELY STIFF STRUCTURE PRODUCED WITH ADDITIVE MANUFACTURING

One of the primary goals of this project is to produce a physical model of the selectively stiff airfoil and demonstrate its capabilities in a mechanical test. This is accomplished through additive manufacturing. The term additive manufacturing encompasses a large number of technologies, including: Selective Laser Sintering (SLS), Stereolithography (SLA), and Fused Deposition Modeling (FDM). FDM is the technology used by most hobbyist 3D printers, and was the primary method of production used in this research. A brief description of FDM is provided in this chapter, as well as the process undertaken to print the final airfoil used for testing. The testing method is outlined, and the final results are presented.

5.1 Fused Deposition Modeling

The process of Fused Deposition Modeling initially involves the heating of a thermoplastic filament. A variety of thermoplastics are used for this purpose. One of the most common is polylactic acid (PLA). PLA comes in both amorphous and semi-crystalline forms, and usually exhibits a melting temperature between 190°C and 200°C . The PLA found in 3D printing filaments often results in parts that are semi-glossy and brittle, so it is typically favored for hobbyists and modeling rather than engineering parts. It is, however, a very low cost material that prints well and easily, resulting in little to no warpage or other undesirable features. This is the primary material used in initial prototypes throughout this project. Other materials common in 3D printing include the engineering plastics acrylonitrile butadiene styrene (ABS), modified polyethylene terephthalate (PET), and nylon, which are often more difficult to use but display better mechanical properties, thermoplastic polyurethane (TPU),

an elastic, flexible material, and polyvinyl alcohol (PVA), a water-soluble polymer found in many household glues that is used as a support material.

The molten thermoplastic is extruded from a nozzle as thin strands onto a planar surface colloquially referred to as a build-plate. The nozzle traces a print path based on a set of instructions provided by a software program known as a slicer, which breaks computer-generated model into a series of layers. The nozzle or the build plate is raised or lowered, respectively, at the completion of a layer providing a new plane on which to print. A part is then progressively built-up layer-by-layer, with each layer being bonded to the previous by the temperature of the molten plastic being extruded from the nozzle.

This inter-layer bonding provides the most notable failure point, and therefore the greatest weakness of the FDM technique. This can be mitigated by orienting a print so that the greatest principal stresses align with the printing plane, as shown in Fig. 5.1. The flexural-reinforced bistable element experienced significant difficulties, however, in that it experienced two failure locations, shown in Fig. 5.2. The greater of these, though, is the corners shared by the flexural members and the curved regions, which are clear stress concentrations. The printing orientation of the embedded element is also ultimately determined by the orientation of the printed airfoil. This was practically determined by the lack of supporting structure for the upper surface. This is another consequence of the layer-by-layer method of FDM. The printer is required to deposit material on a surface, or else the deposited string sags before it has a chance to fully solidify. A sacrificial structure can be printed simultaneously that provides such a surface. This would be extremely impractical for the airfoil, however, resulting in waste several times the weight of the finished product.

A natural aspect of printing on the edge of the part is that the edges of the curved region will be the location of a layer boundary. The consequence of this is the highest stresses as the part snaps-through are located in the weakest location. The proscribed solution to this problem is to replace this sharp corner with a radius to remove the stress concentration. This has only a minor impact, however, since the stress is still

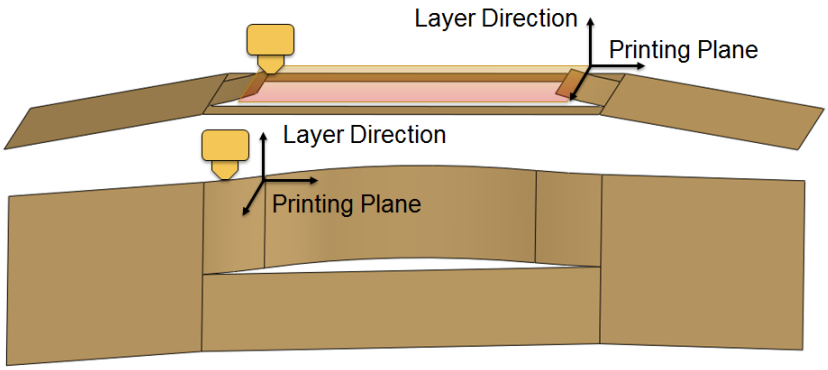

Figure 5.1. Example part in two print orientations.

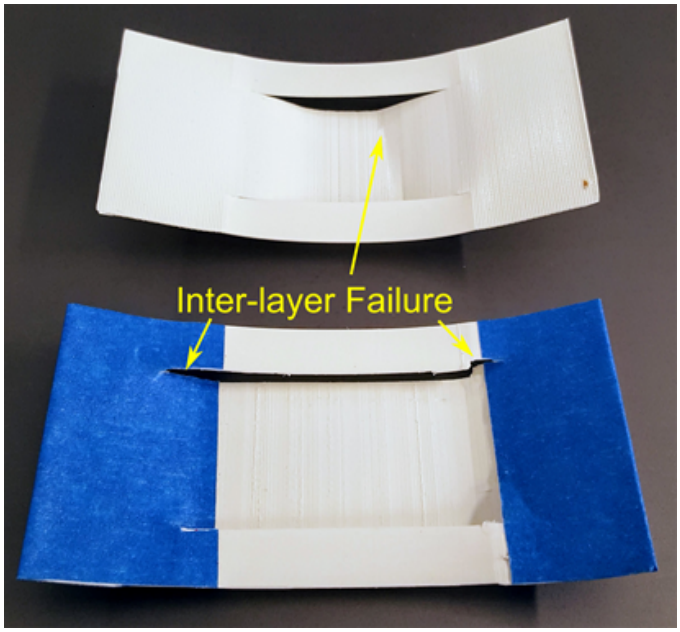

Figure 5.2. Photo showing two failed elements printed in orthogonal directions. Each shows inter-layer failure at different locations of maximum stress.

maximum at some point along the radius, which is itself composed of layers. This allows cracks to easily form and propagate between layers. No satisfactory solution was developed to resolve this problem. A combination of geometry changes and material selection resulted in a working part, as described in the next section.

5.2 Airfoil Manufacturing

Many physical models of the bistable elements and airfoils were produced over the course of this project, as indicated by the 3D-printed elements depicted in Chapter 3. Figure 5.3 shows the progression of technologies and materials used throughout this research. The earliest printed model was produced using an Objet Connex printer. This machine uses inkjet technology to deposit a layer of photo-cured resin. The greatest advantage of this technology is the ability to seamlessly mix materials. The two materials shown in the figure are a rigid plastic (white) and a rubber-like, flexible material (black). The printer was unable to accommodate the thin shells of the bi-stable element, however, which warped significantly.

Further efforts were accomplished using FDM printers. Two printers used in most of the study were a MakerBot Replicator 2, an early hobbyist printer, and an Ultimaker 3 Extended, a dual-extruder, desktop printer. The MakerBot was primarily used for early test models, and its use was phased out by the end of the project. The dual-extrusion feature of the Ultimaker printer was particularly useful as prints transitioned from single-material, typically PLA, to multi-material constructions seeking to take advantage of the combination of different properties.

The final version of the airfoil is shown in Fig. 5.4. This airfoil was produced using a Markforged Mark Two desktop printer. The Markforged printer uses exclusively nylon filaments, with one variety, under the trade name Onyx, containing discontinuous carbon fiber. This material was chosen to print the final model due to its favorable toughness compared to PLA. It also demonstrates qualitatively better inter-layer bonding, possibly due to the elevated temperatures required for printing. Finally, the carbon fiber in the nylon increases the material's stiffness, resulting in an elastic modulus of 1400 MPa, which was the closest to the result specified by the optimizer for the airfoil. The Markforged printer only has one nozzle for plastic material, however, so the element also had to be printed with the same material.

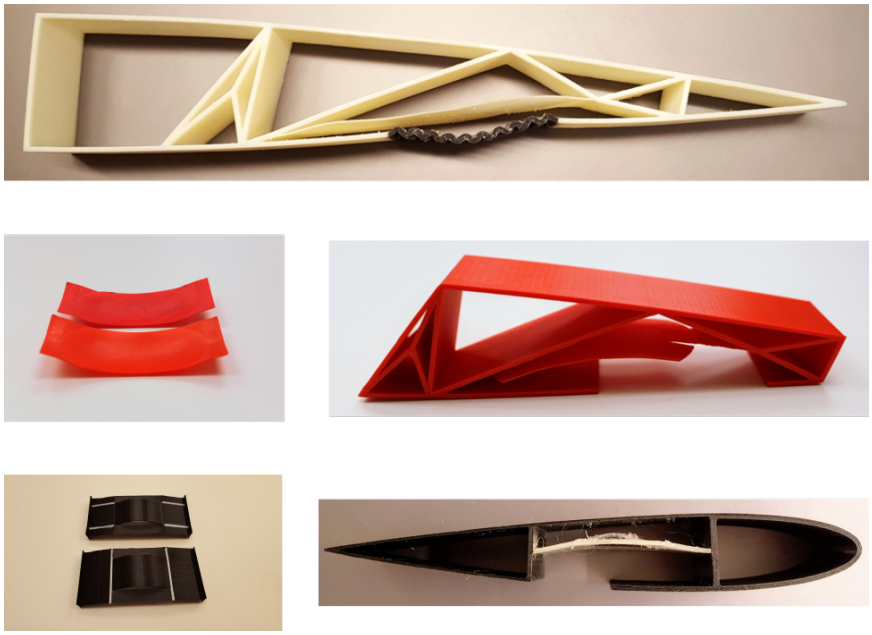

Figure 5.3. Photos showing progression of printed models starting from photo-cured resin (top) through single-material FDM parts (middle) to multi-material FDM parts (bottom).

A number of other changes were also made to the printed model. Most of the thicknesses provided by the optimizer could not be printed as is due to the discrete nozzle diameter of the printer. The thickness values were therefore adjusted to realistic values. The overall width and planar region width were both slightly increased, and the curve height was decreased. This was meant to decrease the activation energy of the snap-through and increase the difference between activation energy and stable energy at State 2. The overall effect was to increase the stability of the element while lowering stress during snap-through and reducing the chance of cracking. The final change was the addition of a reinforcing structure in the T.E. region of the airfoil. It was observed in early iterations of the final design that the airfoil skin in this region tended to buckle when the T.E. was deflected, an undesirable trait that also reduced the effectiveness of the element. The reinforcement serves to localize the loads on the T.E. and transfer them to the box containing the bi-stable element.

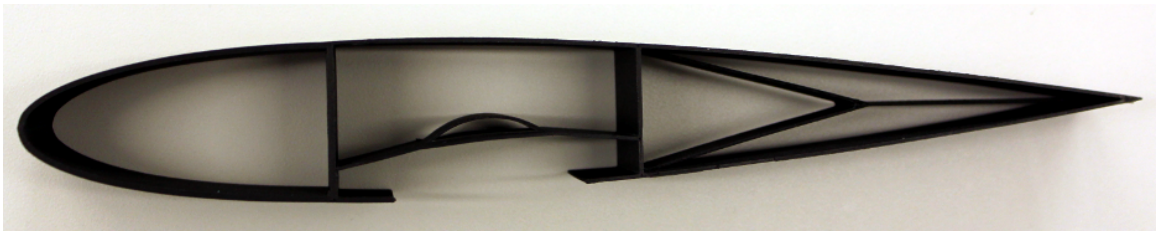

Figure 5.4. Photo of the final printed airfoil.

5.3 Mechanical Testing

The final printed model is tested using an Instron 3345 tensile testing machine. A fixture is designed to constrain the D-spar region and printed out of ABS. The fixture uses a drafted version of the inner profile of the D-spar to accommodate varying shell thicknesses. This feature then acts as a clamp to prevent movement of the D-spar edges, in order to simulate the boundary conditions used in the FEA. This setup is shown in Fig. 5.5. The airfoil is cantilevered over the center axis of the testing machine and a rounded tool is used to deliver a compressive load on the T.E. using the crosshead of the machine. The reaction force as the T.E. is deflected is measured using a 100 N load cell. A testing program is written for the machine to deflect the T.E. by 15 mm at 10 mm/min.

The airfoil is tested in the first, stress-free state. The element is then snapped into its second state. This snap-through deforms the rib, which requires the displacement of the crosshead to be re-zeroed before the test is repeated for the second state. The results of this test on the final printed model are shown in Fig. 5.6. The maximum slope shows the stiffness of the second state is twice that of the first state. This is notably different than the projection of the optimized model, however, the value compared in that study was the final deflection, not truly the stiffness. An increase of approximately five times is observed when comparing the final reaction forces in

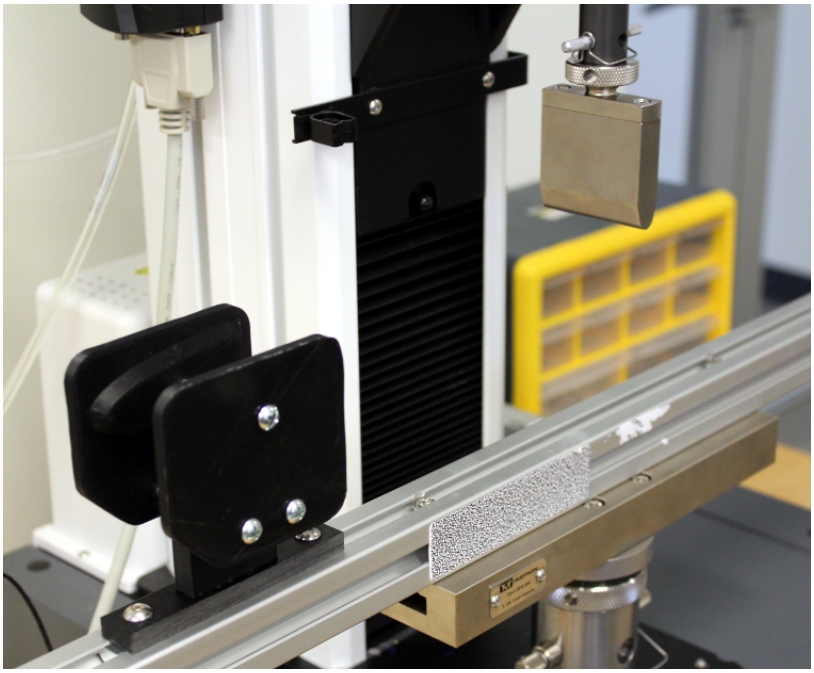

Figure 5.5. Photo of the printed airfoil in mechanical testing fixture.

the mechanical test, which is much closer to the optimized prediction. Some loss is to be expected, considering the modifications made to the final model.

Figure 5.7 shows the undeformed and deformed states of the rib in each element state. Figure 5.7(c) in particular shows the distortion of the rib caused by switching the element. This is certainly an undesirable trait, however, this could be accounted for in future models with a more rigorous tailoring and optimization process. The images in the figure demonstrate the asymmetric buckling discussed in Section 2.2, which provides the difference in stiffness observed during the test.

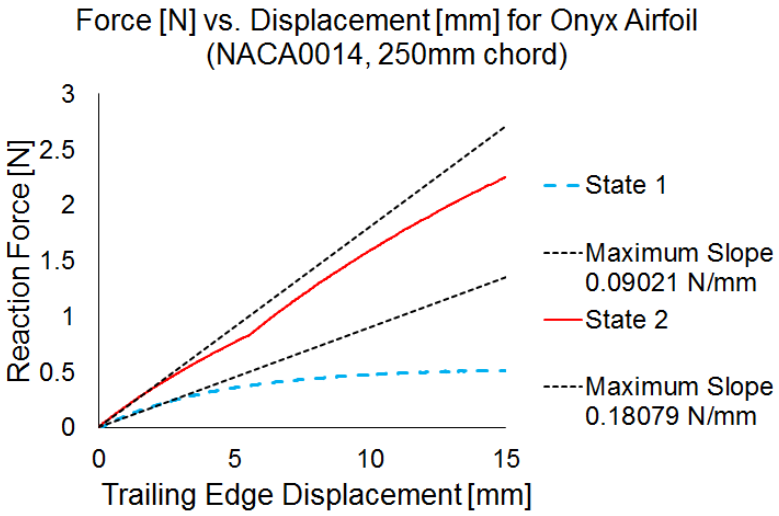

Figure 5.6. Plot of the results from mechanical testing of the airfoil. The maximum calculated slope is shown for each state.

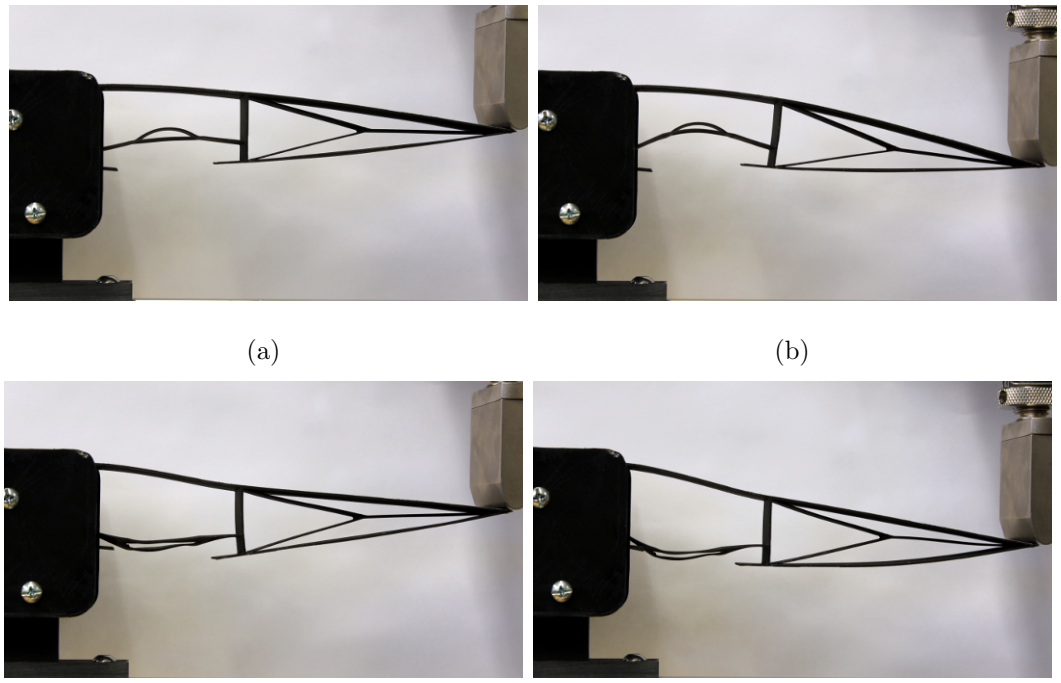

(a) (b)

(c) (d)

Figure 5.7. Photos of the (a) undeformed and (b) deformed airfoil in State 1, and (c) undeformed and (b) deformed airfoil in State 2. Deformed states undergo T.E. deflection of 15 mm.

6. CONCLUSIONS

The primary goal for this project is to design, manufacture, and test a morphing airfoil concept that demonstrates the principle of selective stiffness. The model shown in Chapter 5 is an early-phase prototype of such an airfoil. It demonstrates how local stiffness changes can be accomplished to affect the global structural properties. This is achieved through the application of locally bi-stable elements. Three such elements are developed and explored throughout the project. The element showing the greatest promise, using an arch-like structure reinforced by flexural members, is embedded in a parametric airfoil model. This model is then optimized through the location and geometry of the element and the properties of the airfoil to demonstrate a maximum of stiffness change between states of the element.

In the exploration of the elements, an initial model is proposed utilizing a variable curvature in a single direction. It is apparent that this model lacks geometric bi-stability; however, it demonstrates the potential to use pre-strain to induce bi-stability in a stress-free model. Further exploration of creating this pre-strain through the application of a shrinking layer proves that this is an impractical idea, particularly compared to the simplicity of producing a fully-monolithic structure with geometric bi-stability. The focus of the project shifts as a result to more arch- or dome-like structures with more well-proven stability characteristics.

The work presented here shows that geometrically bi-stable elements have potential as selectively stiff members in a truss-like structure. The selective stiffness concept is also again proven to be able to alter the compliance of a morphing rib structure. The application of this principle in future efforts promises to open up the design space in the field of morphing wings.

6.1 Future Work

Some areas for potential further work include:

- Further development of ideal topologies for selectively stiff elements using geometric bi-stability. The geometries presented here are by no means exhaustive, and a more methodical, mathematically-driven approach could reveal novel shapes yielding significantly improved characteristics.

- A study on the mechanics of layer bonding and separation in additive manufacturing could be undertaken. This could also incorporate research into the effects of various process controls on the overall product quality.

- As discussed, the optimization process for the selectively stiff airfoil encountered significant difficulty using the response surface methodology. A more optimal solution could likely exist. Another method, such as Covariant Matrix Adaptive Evolutionary Strategies might be better suited to this type of problem. Further efforts in this area could also better incorporate the stability of the element.

- A more comprehensive aeroelastic study of the optimized rib also remains to be undertaken. Incorporating multiple ribs and a compliant skin into a finite wing simulation is one objective of this investigation. A section of such a wing could also be built and tested in a wind tunnel.

REFERENCES

[1] John Conti, Paul Holtberg, Jim Diefenderfer, Angelina LaRose, James T. Turnure, and Lynn Westfall. International Energy Outlook 2016 With Projections to 2040. Technical report, 2016.

[2] FAA. FAA aerospace forecast fiscal years 2018-2038. Technical report, Federal Aviation Administration, 2017.

[3] Izabela K. Kuder, Andres F. Arrieta, and Paolo Ermanni. Design space of embeddable variable stiffness bi-stable elements for morphing applications. *Composite Structures*, 122:445–455, 2015.

[4] Orville Wright and Wilbur Wright. Flying-Machine, 1906.

[5] L. F. Campanile. Lightweight Shape-Adaptable Airfoils: A New Challenge for an Old Dream. In *Adaptive Structures: Engineering Applications*. 2007.

[6] Terrence A. Weisshaar. Morphing Aircraft Systems: Historical Perspectives and Future Challenges. *Journal of Aircraft*, 50(2):337–353, 2013.

[7] Alexander Albert Holle. Plane and the Like for Aeroplanes, 1917.

[8] William Ray Parmele. Wing construction for aeroplanes, 1931.

[9] A. Hasse, I. Zuest, and L. F. Campanile. Modal synthesis of belt-rib structures. *Proceedings of the Institution of Mechanical Engineers, Part C: Journal of Mechanical Engineering Science*, 225:722–732, 2011.

[10] S. M. Ehlers and Terrence A. Weisshaar. Static aeroelastic behavior of an adaptive laminated piezoelectric composite wing. *31st Structures, Structural Dynamics and Materials Conference*, 1990.

[11] Boris A. Grohmann, Christoph Maucher, Tobias Prunhuber, Peter Jänker, Oliver Dieterich, Bernhard Enenkl, Markus Bauer, Elif Ahci, Andree Altmikus, and Horst Baier. Multidisciplinary design and optimization of active trailing edge for smart helicopter rotor blade. *Mechanics of Advanced Materials and Structures*, 15(3-4):307–324, 2008.

[12] Alexander Hasse and Flavio Campanile. Compliant mechanisms with selective compliance. *Smart Materials and Structures*, 18, 2009.

[13] Kenneth Cheung, Daniel Cellucci, Grace Copplestone, Nick Cramer, Jesse Fusco, Ben Jenett, Joseph Kim, Alexandra Langford, Alex Mazhari, Greenfield Trinh, Tyler Clinkaberry, Olivia Formoso, and Sean Shan-Min Swei. Development of Mission Adaptive Digital Composite Aerostructure Technologies (MADCAT). *17th AIAA Aviation Technology, Integration, and Operations Conference*, (June):1–14, 2017.

[14] F. Runkel, A. Reber, G. Molinari, A. F. Arrieta, and P. Ermanni. Passive twisting of composite beam structures by elastic instabilities. *Composite Structures*, 147:274–285, 2016.

[15] Falk Runkel, Giulio Molinari, Andres F. Arrieta, and Paolo Ermanni. Shape Adaptation of Wing Structures by Chiral Structures Undergoing Elastic Instability. *25th AIAA/AHS Adaptive Structures Conference*, (January):1–10, 2017.

[16] D. Matthew Boston, Andres F. Arrieta, and Jose Rivas-Padilla. Monolithic morphing rib with selective stiffness from embeddable bi-stable elements. In *Proceedings of the ASME 2018 Conference on Smart Materials, Adaptive Structures and Intelligent Systems*, San Antonio, TX, 2018. American Society of Mechanical Engineers.

[17] Izabela K. Kuder, Andres F. Arrieta, Mathias Rist, and Paolo Ermanni. Aeroelastic response of a selectively compliant morphing aerofoil featuring integrated variable stiffness bi-stable laminates. *Journal of Intelligent Material Systems and Structures*, 27(14):1949–1966, 2016.

[18] Andres F. Arrieta, Onur Bilgen, Michael I. Friswell, and Peter Hagedorn. Dynamic control for morphing of bi-stable composites. *Journal of Intelligent Material Systems and Structures*, 24(3):266–273, 2013.

[19] Michael W Hyer. Calculations of the Room-Temperature Shapes of Unsymmetric Laminates. *Composite Materials*, 15:296–310, 1981.

[20] S. D. Guest and S. Pellegrino. Analytical models for bistable cylindrical shells. *Proceedings of the Royal Society A: Mathematical, Physical and Engineering Sciences*, 462:839–854, 2006.

[21] S. Daynes, K. D. Potter, and P. M. Weaver. Bistable prestressed buckled laminates. *Composites Science and Technology*, 68:3431–3437, 2008.

[22] Kevin D. Potter and Paul M. Weaver. A concept for the generation of out-of-plane distortion from tailored frp laminates. *Composites Part A: Applied Science and Manufacturing*, 35:1353–1361, 2004.

[23] Jong Gu Lee, Junghyun Ryu, Seung Won Kim, Je Sung Koh, Kyu Jin Cho, and Maenghyo Cho. Effect of initial tool-plate curvature on snap-through load of unsymmetric laminated cross-ply bistable composites. *Composite Structures*, 122:82–91, 2015.

[24] Tian Chen, Osama R Bilal, Kristina Shea, and Chiara Daraio. Harnessing bistability for directional propulsion of soft, untethered robots. *Proceedings of the National Academy of Sciences of the United States of America*, 115(22):5698–5702, may 2018.

[25] Young Seok Oh and Sridhar Kota. Synthesis of Multistable Equilibrium Compliant Mechanisms Using Combinations of Bistable Mechanisms. *Journal of Mechanical Design*, 131, 2009.

[26] Marco Amabili. *Nonlinear vibrations and stability of shells and plates*. 2008.

[27] A. D. Norman, K. A. Seffen, and S. D. Guest. Morphing of curved corrugated shells. *International Journal of Solids and Structures*, 46(7-8):1624–1633, 2009.

[28] Keith A. Seffen and Stefano Vidoli. Eversion of bistable shells under magnetic actuation: A model of nonlinear shapes. *Smart Materials and Structures*, 25(6), 2016.

[29] E. Kebadze, S. D. Guest, and S. Pellegrino. Bistable prestressed shell structures. *International Journal of Solids and Structures*, 41(11-12):2801–2820, 2004.

[30] M. Santer and S. Pellegrino. Compliant multistable structural elements. *International Journal of Solids and Structures*, 45(24):6190–6204, 2008.

[31] Tyge Schioler and Sergio Pellegrino. Space Frames with Multiple Stable Configurations. *AIAA Journal*, 45(7):1740–1747, 2007.

[32] Andres F. Arrieta, Izabela K. Kuder, Tobias Waeber, and Paolo Ermanni. Variable stiffness characteristics of embeddable multi-stable composites. *Composites Science and Technology*, 97:12–18, 2014.

[33] Izabela K. Kuder, Andres F. Arrieta, Mathias Rist, and Paolo Ermanni. Static Design of a Selective Compliance Morphing Wing Profile Based on Integrated Variable Stiffness Bi-Stable Components. In *Volume 1: Development and Characterization of Multifunctional Materials; Modeling, Simulation and Control of Adaptive Systems; Structural Health Monitoring; Keynote Presentation*. ASME, sep 2014.

[34] A. Bilanin and R. McKillip. Actuating device with at least three stable positions, 2002.

[35] Dassault Systemes Simulia Corp. Abaqus. Technical report, 2012.

[36] Izabela K. Kuder, Urban Fasel, Paolo Ermanni, and Andres F. Arrieta. Concurrent design of a morphing aerofoil with variable stiffness bi-stable laminates. *Smart Materials and Structures*, 25(11), 2016.

[37] D. Matthew Boston and Andres F. Arrieta. Design of monolithic selectively compliant morphing structures with locally bistable elements. In *2018 AIAA/AHS Adaptive Structures Conference, AIAA SciTech Forum*, Kissimee, Florida, 2018. American Institute of Aeronautics and Astronautics.

[38] Douglas C. Montgomery. *Design and Analysis of Experiments*. John Wiley & Sons, 8th edition, 2013.

[39] The MathWorks, Inc. MATLAB and Optimization Toolbox, 2015.